

Kinetic theory of two-dimensional point vortices at order $1/N$ and $1/N^2$

Jean-Baptiste Fouvry¹ and Pierre-Henri Chavanis²

¹*Institut d'Astrophysique de Paris, UMR 7095, 98 bis Boulevard Arago, F-75014 Paris, France*

²*Laboratoire de Physique Théorique, Université de Toulouse, CNRS, UPS, France*

We investigate the long-term relaxation of a distribution of N point vortices in two-dimensional hydrodynamics. To focus on the regime of weak collective amplification, we embed these point vortices within a static background potential and soften their pairwise interaction on small scales. Placing ourselves within the limit of an average axisymmetric distribution, we stress the connections with generic long-range interacting systems, whose relaxation is described within angle-action coordinates. In particular, we emphasise the existence of two regimes of relaxation, depending on whether the system's profile of mean angular velocity (frequency) is a non-monotonic [resp. monotonic] function of radius, which we refer to as profile (1) [resp. profile (2)]. For profile (1), relaxation occurs through two-body non-local resonant couplings, i.e. $1/N$ effects, as described by the inhomogeneous Landau equation. For profile (2), the impossibility of such two-body resonances submits the system to a “kinetic blocking”. Relaxation is then driven by three-body couplings, i.e. $1/N^2$ effects, whose associated kinetic equation has only recently been derived. For both regimes, we compare extensively the kinetic predictions with large ensemble of direct N -body simulations. In particular, for profile (1), we explore numerically an effect akin to “resonance broadening” close to the extremum of the angular velocity profile. Quantitative description of such subtle nonlinear effects will be the topic of future investigations.

I. INTRODUCTION

Two-dimensional ($2D$) geophysical and astrophysical flows have the striking property of organising spontaneously into coherent structures (large-scale vortices) [1, 2]. A famous example of this self-organization is Jupiter's great red spot. Since these coherent structures result from a turbulent mixing, it has sometimes been said that “order emerges from chaos”. To account for this self-organization, Onsager [3] considered the statistical mechanics of a system of point vortices of circulations γ_i ($i=1, \dots, N$) on the plane. He showed the existence of negative temperature states¹ at which point vortices of the same sign tend to group themselves into “supervortices”. His qualitative arguments were later developed by Joyce and Montgomery [5, 6], Kida [7] and Pointin and Lundgren [8, 9] in a mean field approximation valid for $N \rightarrow +\infty$, with $\gamma \sim 1/N$. Overall, this leads to the Boltzmann distribution coupled to the Poisson equation.² This equilibrium state (most probable state) can be obtained by maximising the Boltzmann entropy at fixed circulation, energy, and angular momentum. Later, Miller [11], as well as Robert and Sommeria [12], considered the statistical mechanics of more realistic continuous vorticity fields (instead of singular point vortices) described by the $2D$ Euler–Poisson equations. In par-

ticular, they derived a generalization of the Boltzmann distribution involving a continuum of vorticity levels. For a long time, the distinction between these two statistical theories was not fully understood and appreciated. It was clarified only later by developing the analogy between $2D$ vortices and stellar systems [1, 13].

Indeed, self-gravitating systems also self-organize into coherent structures like star clusters, galaxies, or even clusters of galaxies [14]. Stellar systems, which are fundamentally discrete (i.e. made of a collection of N stars in gravitational interaction), undergo two successive types of evolution. In a first regime, one can ignore gravitational encounters between stars and make a mean field approximation. In this collisionless regime, the locally averaged distribution function of stellar systems is governed by the Vlasov–Poisson equations. Collisionless stellar systems generically experience a process of violent relaxation towards a quasistationary (virialised) state which is a stable stationary solution of the Vlasov–Poisson equations. Lynden-Bell [15] tried to predict this quasistationary state in terms of statistical mechanics but his prediction is spoiled by the problem of incomplete relaxation [15, 16]. Then, on longer timescales, stellar systems evolve under the effect of gravitational encounters (finite- N effects, granularities, correlations...). During this collisional regime, stellar systems have the tendency to become isothermal but their relaxation towards a true statistical equilibrium state described by the Boltzmann–Poisson equation³ is hampered by phys-

¹ This was a few years before the discovery of negative temperature states in nuclear spin systems [4]. In his visionary paper, Onsager also predicted, in a famous footnote, the quantization of the circulation of point vortices in units of h/m in superfluid helium.

² In unpublished notes [10], Onsager had previously developed this mean field theory by analogy with his research on electrolytes, which are also described by the Boltzmann–Poisson equations.

³ Actually, there is no statistical equilibrium state for self-gravitating systems in $3D$ because the Boltzmann distribution coupled to the Poisson equation has an infinite mass. Said differently, there is no maximum entropy state at fixed mass and energy.

ical effects such as the evaporation of high energy stars and the gravothermal catastrophe (core collapse) [17].

Similar results apply to $2D$ vortices. A gas of point vortices, like a gas of stars, undergoes two successive types of evolution. In a first regime, one can ignore finite- N effects and make a mean field approximation. In this collisionless limit, the locally averaged vorticity of $2D$ point vortices is governed by the $2D$ Euler–Poisson equations. Collisionless point vortices generically experience a process of violent relaxation towards a quasistationary state which is a stable stationary solution of the $2D$ Euler–Poisson equations. The Miller–Robert–Sommeria [11, 12] statistical theory in fluid mechanics, which applies to this regime, is the counterpart of the Lynden-Bell theory [15] in stellar dynamics. Its predictions are also affected by the problem of incomplete relaxation. Then, on longer timescales (collisional regime), $2D$ point vortices, just like stellar systems, evolve under the effect of “collisions” towards the statistical equilibrium state described by the Boltzmann–Poisson equation [5–9].

One can then develop the kinetic theory of $2D$ point vortices by analogy with the kinetic theory of stellar systems pioneered by Chandrasekhar [18–21]. By making a thermal bath approximation and using the methods of Brownian theory [22], Chandrasekhar showed that a test star experiences a stochastic process governed by a Fokker–Planck equation involving a diffusion term and a friction term. Similarly, under the same assumptions, a test vortex experiences a stochastic process governed by a Fokker–Planck equation involving a diffusion term and a drift term [23, 24]. As such, the drift of a point vortex is the counterpart of the dynamical friction undergone by a star. These Fokker–Planck equations relax both towards the Boltzmann distribution. In addition, the diffusion and friction (or drift) coefficients are related to each other and to the temperature through some Einstein relation. In particular, in the case of point vortices, the temperature may be negative.

However, this thermal bath approach is oversimplified and does not correctly describe the collisional evolution of the system as a whole. In particular, the Fokker–Planck equation does not conserve the total energy. A better kinetic equation for systems with long-range interactions is the Landau equation [25] or the Balescu–Lenard equation [26, 27] which were originally introduced for homogeneous plasmas and applied in a slightly different form to stellar systems by making a local approximation [28]. These kinetic equations take into account two-body correlations (collisions), so they are valid at order $1/N$. In the homogeneous case, they relax towards the Maxwell–Boltzmann distribution on a timescale $(N/\ln N)T_{\text{dyn}}$, due to logarithmic corrections. These kinetic equations were later extended to describe the axisymmetric evolution of a point vortex gas as a whole [24, 29–37]. It turns out that their structure is seemingly different from the original (homogeneous) Landau and Balescu–Lenard equations. Indeed, they involve a resonance condition on

the profile of angular velocity $\Omega(r, t)$. As long as the profile of angular velocity is non-monotonic, the resonance condition can be satisfied and the system relaxes through two-body effects. However, the relaxation stops when the profile of angular velocity becomes monotonic, even if the system has not reached the statistical equilibrium state. This is an example of “kinetic blocking” [24, 31]. A similar situation of kinetic blocking had been previously observed for $1D$ homogeneous plasmas [38]. In that case, the Balescu–Lenard collision term vanishes identically and the evolution of the system is governed by a collision term of order $1/N^2$ that accounts for three-body correlations. An explicit expression for this collision term has been obtained recently in the case of homogeneous $1D$ systems with long-range interactions, when collective effects are neglected [39, 40]. It always drives the relaxation towards the Boltzmann distribution, showing that the relaxation time scales as $N^2 T_{\text{dyn}}$ in that case.

In reality, stellar systems are spatially inhomogeneous. Their kinetic theory is described by the inhomogeneous Balescu–Lenard equation written with angle-action variables [41, 42]. When collective effects are neglected (i.e. for sufficiently hot systems), it reduces to the inhomogeneous Landau equation [43]. These equations involve a resonance condition that depends on the orbital frequencies, $\Omega(\mathbf{J}, t)$, which themselves are functions of the actions, \mathbf{J} . This is similar to the kinetic equation for $2D$ point vortices with more general variables. For $1D$ inhomogeneous long-range interacting systems with a monotonic frequency profile in which only 1:1 resonances are permitted, there can also be a kinetic blocking, just like for axisymmetric point vortices. In that case, one has to develop the kinetic theory at the order $1/N^2$. The expression of the collision term in the absence of collective effects has been obtained in [44]. Except for very special interaction potentials [45], this equation drives the system towards the Boltzmann distribution on a timescale $N^2 T_{\text{dyn}}$.

Building upon this rich history of parallel theoretical developments, in the present work, we leverage the generality of the kinetic theory of (inhomogeneous) long-range interacting systems to apply it to describe the long-term relaxation of axisymmetric distribution of point vortices.

First, we focus on a case with a non-monotonic distribution of orbital frequency (i.e. the vortices’ angular velocity) [profile (1)]. To place ourselves in the limit where collective effects can be neglected, we embed the point vortices within a static background potential and soften the pairwise interaction on small scales. In that case, relaxation can be described with the inhomogeneous Landau equation. We compare quantitatively its prediction with measurements in direct N -body simulations, focusing in particular on the dependence of the relaxation rate with the total number of particles and their active fraction (i.e. the fraction of self-consistency in the mean potential). Importantly, we unveil how, close to the extremum of the angular velocity profile, the effective relaxation in the N -body simulations is reduced

compared to the kinetic prediction. We attribute this effect to “resonance broadening” through nonlinear effects and present a heuristic correction to the Landau equation that closely matches the numerical measurements. Surprisingly, we show that as one delays the impact of nonlinearities, e.g., by increasing the number of particles and/or lowering the active fraction, the resonance broadening seems to saturate and the convergence toward the Landau prediction halts.

Second, we focus on the case of an axisymmetric distribution of point vortices with a monotonic distribution of orbital frequency. In that case, both the $1/N$ Landau and $1/N$ Balescu–Lenard equations predict a vanishing flux: a “kinetic blocking” [see, e.g., 24, 31]. Once again, we place ourselves in the limit of weak collective amplification by embedding the point vortices within a static background potential and by softening their pairwise interaction on small scales. In that dynamically hot regime, we compare quantitatively measurements of the relaxation rate in numerical simulations with the prediction from the recently derived $1/N^2$ Landau equation [44]. We obtain a satisfying agreement between both, recovering in particular the appropriate dependence with respect to the total number of particles and their active fraction.

The paper is organised as follows. In Section II, we detail our system. In Section III, we investigate long-term dynamics as driven by $1/N$ effects [profile (1)], while in Section IV, focusing on systems undergoing a kinetic blocking [profile (2)], we consider $1/N^2$ effects. We conclude in Section V. Throughout the main text, technical details are kept to a minimum and deferred to Appendices or to relevant references.

II. SYSTEM

A. Hamiltonian

We consider a $2D$ system composed of N point vortices of individual circulation $\gamma_i = \Gamma_{\text{tot}}/N$, with Γ_{tot} the system’s total active circulation. The dynamics of these vortices is given by the Kirchhoff–Hamilton equations [46]

$$\gamma_i \frac{dx_i}{dt} = \frac{\partial H_{\text{tot}}}{\partial y_i}, \quad \gamma_i \frac{dy_i}{dt} = -\frac{\partial H_{\text{tot}}}{\partial x_i}, \quad (1)$$

with $(x_i, y_i) = \mathbf{r}_i$ the location of the point vortex i . Here, as visible in Eq. (1), x_i and y_i should be interpreted as canonically conjugate. The system’s total Hamiltonian is

$$H_{\text{tot}} = \sum_{i < j} \gamma_i \gamma_j U(\mathbf{r}_i, \mathbf{r}_j), \quad (2)$$

with the pairwise interaction

$$U(\mathbf{r}, \mathbf{r}') = -\frac{G}{2\pi} \ln |\mathbf{r} - \mathbf{r}'| \quad (3)$$

of typical amplitude G . We point out that H_{tot} does not contain any kinetic energy term in the usual

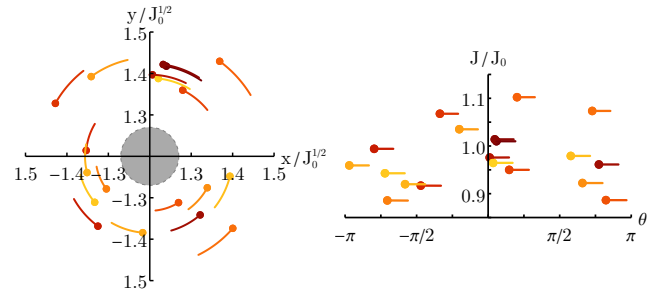


FIG. 1: Left: Illustration in configuration space, (x, y) , of the dynamics of a few point vortices following the DF from Eq. (6). Right: Same, but in action space (θ, J) . In that space, the vortices follow (perturbed) straight-line trajectories.

sense. We also recall that the $2D$ Newtonian potential U from Eq. (3) satisfies the Poisson equation $\Delta_{\mathbf{r}} U(\mathbf{r}, \mathbf{r}') = -G \delta_{\text{D}}(\mathbf{r} - \mathbf{r}')$.

In practice, to cure possible divergences on small scales in Eq. (3), we replace the pairwise interaction with its softened analog

$$U_{\epsilon}(\mathbf{r}, \mathbf{r}') = -\frac{G}{2\pi} \ln (|\mathbf{r} - \mathbf{r}'|^2 + \epsilon^2)^{1/2}, \quad (4)$$

with ϵ some (small) softening length. This greatly eases the implementation of the N -body simulations (see Appendix G).

B. Axisymmetric limit

When averaged over independent realisations, the system’s statistics is described via its distribution function (DF), $F = F(\mathbf{r}, t)$, normalised to $\int d\mathbf{r} F = \Gamma_{\text{tot}}$. We assume that the mean DF, $F(\mathbf{r}, t) = \langle \sum_i \gamma_i \delta_{\text{D}}[\mathbf{r} - \mathbf{r}_i(t)] \rangle$ is axisymmetric so that one has $F = F(r, t)$ with $r = |\mathbf{r}|$. Subsequently, the mean individual Hamiltonian $H(\mathbf{r}, t) = \int d\mathbf{r}' U(\mathbf{r}, \mathbf{r}') F(\mathbf{r}', t)$ is $H = H(r, t)$. We can then introduce appropriate angle-action coordinates (θ, J) , with θ the 2π -periodic angle and J the associated action, via⁴

$$\theta = \tan^{-1}(x/y), \quad J = \frac{1}{2} r^2. \quad (5)$$

Importantly, volume conservation ensures that $d\mathbf{r} = d\theta dJ$. With such a choice, it is now clear how an axisymmetric distribution of point vortices can simply be interpreted as one example of a long-range interacting inhomogeneous systems [see, e.g., 42], characterised by some mean DF, $F = F(J, t)$. Along the same line, from the mean Hamiltonian, $H = H(J, t)$, we define the

⁴ These follow from the generating function $S(y, \theta) = \frac{1}{2} y^2 \tan \theta$, to be used in eq. (D.94) of [14].

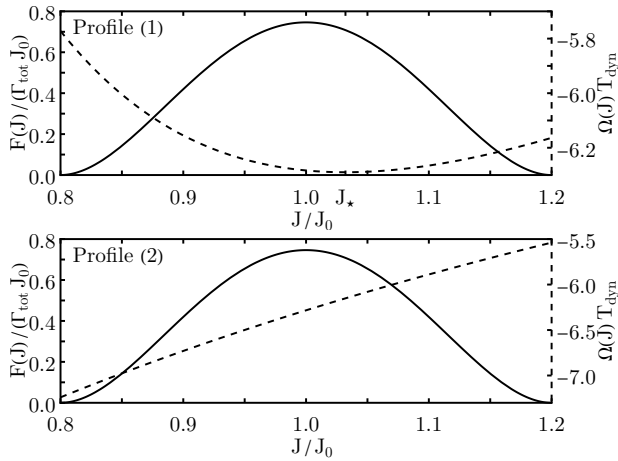


FIG. 2: Illustration of the DF from Eq. (6) (full lines) and the considered frequency profiles (dashed lines). Profile (1) (top panel) is non-monotonic and has an extremum in $J_* = 1.03 J_0$, while profile (2) (bottom panel) is monotonic.

mean orbital frequency, $\Omega(J, t) = \partial H / \partial J$.⁵ In Fig. 1, we illustrate the typical evolution in configuration space and action space of such axisymmetric distributions. The goal of kinetic theory is to describe the mean long-term evolution of the orbital distribution, i.e. to predict $\partial F(J, t) / \partial t$. Let us now describe the setup considered in this work.

C. Initial conditions

For the DF, we consider an initial condition of the form

$$F(J) = A \left(\frac{J - J_0}{\sigma_0} + 1 \right)^2 \left(\frac{J - J_0}{\sigma_0} - 1 \right)^2 \Theta[|J - J_0| \leq \sigma_0], \quad (6)$$

with $\Theta[x \geq 0]$ the usual Heaviside function and $A = 15 \Gamma_{\text{tot}} / (32 \pi \sigma_0)$ to ensure $\int dJ d\theta F = \Gamma_{\text{tot}}$. As illustrated in Fig. 2, this DF is characterised by two parameters, namely J_0 its central location and σ_0 its width. This DF is non-zero only within the domain $|J - J_0| \leq \sigma_0$ and is continuous, along with its first derivative, on the entire action domain. As such, it is a convenient DF with which to explore long-term relaxation.

⁵ In the original point vortex model [see, e.g., 34], the DF $F(\mathbf{r}, t)$ corresponds to the vorticity $\omega(\mathbf{r}, t)$, the individual Hamiltonian $H(\mathbf{r}, t)$ corresponds to the stream function $\psi(\mathbf{r}, t)$, and the orbital frequency $\Omega(J, t)$ corresponds to the angular velocity $\Omega(r, t)$ (for axisymmetric flows). For the 2D Newtonian interaction potential, one has $\omega = -\Delta\psi$ and $\Omega(r, t) = \frac{1}{r^2} \int_0^r dr' r' \omega(r', t)$.

D. Active fraction

To limit ourselves to the dynamically hot limit, i.e. the limit of small amplification of perturbations, we assume that part of the Hamiltonian is not self-consistently generated by the vortices. As such, we introduce an active fraction, $0 < q < 1$, and make the replacement

$$\gamma_i \rightarrow q \gamma_i, \quad (7)$$

so that the total circulation $\Gamma_{\text{tot}} = \sum_{i=1}^N \gamma_i$ is also reduced by a factor q . Following this modification, we add an external potential to our system to ensure that systems with different N and q share the exact same mean-field orbital frequencies.

More precisely, we replace the total Hamiltonian from Eq. (2) with

$$H_{\text{tot}} = \sum_{i=1}^N \gamma_i U_{\text{ext}}(\mathbf{r}_i) + \sum_{i < j}^N \gamma_i \gamma_j U_{\epsilon}(\mathbf{r}_i, \mathbf{r}_j). \quad (8)$$

In that expression, U_{ϵ} is the softened pairwise interaction from Eq. (4). We also introduced an external potential, U_{ext} , that reads

$$U_{\text{ext}} = H_0 - H_{\epsilon}[F]. \quad (9)$$

In that expression, $H_{\epsilon}[F](\mathbf{r}) = \int d\mathbf{r}' F(\mathbf{r}', t=0) U_{\epsilon}(\mathbf{r}, \mathbf{r}')$ is the (softened) potential generated by the initial DF from Eq. (6). We also introduced $H_0 = H_0(J)$ an axisymmetric external potential. Importantly, with the present choice, at $t=0$, we have $\langle H_{\text{tot}} \rangle = \sum_i \gamma_i H_0(J)$, i.e. the initial mean-field orbital frequencies are simply $\Omega(J) = dH_0/dJ$. From it, we also define the dynamical time as $T_{\text{dyn}} = 2\pi / |\Omega(J_0)|$. With this setup, changing the value of N amounts to changing the amplitude of the Poisson fluctuations, while changing q amounts to changing the dynamical temperature, i.e. the level of self-consistent amplification in the system. Indeed, the smaller q , the less the point vortices contribute themselves to the overall total Hamiltonian. Importantly, changing N or changing q does not lead to any change in the mean frequency profile. In the following, for simplicity, we assume that the point vortices have the same circulation, $\gamma_i = \gamma$.

E. Frequency profiles

For the frequency profiles, we consider two different cases, profiles (1) and (2), as illustrated in Fig. 2. As detailed in Appendix A, these correspond to the (unsoftened) potential generated by a simple axisymmetric background distribution (Eq. A2).⁶ The main difference

⁶ We emphasise that the orbital frequency (angular velocity) profile $\Omega(J)$ is not self-consistently generated by the point vortices

between these two frequency profiles, $J \mapsto \Omega(J)$, is that profile (1) is non-monotonic, exhibiting a minimum in $J_* \simeq 1.03 J_0$, while profile (2) is monotonic. As the upcoming section will detail, this difference plays a crucial role in defining the system's regime of relaxation.

III. $1/N$ DYNAMICS

A. Kinetic equation

First, let us consider profile (1). At order $1/N$, relaxation is driven by two-body effects. In the limit where collective effects can be neglected, this is described by the $1/N$ inhomogeneous Landau equation [see, e.g., 43]. In the present context, it reads

$$\frac{\partial F(J, t)}{\partial t} = \gamma \frac{\partial}{\partial J} \left[\sum_k k \int dJ_1 |\Lambda_k(\mathbf{J})|^2 \times \delta_D(\mathbf{k} \cdot \boldsymbol{\Omega}) \mathbf{k} \cdot \frac{\partial}{\partial \mathbf{J}} F_2(\mathbf{J}) \right], \quad (10)$$

where we dropped the time dependence for clarity. We refer to Appendix D for the expression of the coupling coefficients, $|\Lambda_k(\mathbf{J})|^2$, which are independent of both N and q . In Eq. (10), notations are shortened with the 2-vectors $\mathbf{J} = (J, J_1)$, $\boldsymbol{\Omega} = (\Omega[J], \Omega[J_1])$, and $\mathbf{k} = (k, -k)$, as well as $F_2(\mathbf{J}) = F(J)F(J_1)$. When accounting for collective effects, Eq. (10) becomes the inhomogeneous Balescu–Lenard equation [41, 42]. The functional form of Eq. (10) remains the exact same, and one only has to replace the bare coupling coefficients, $|\Lambda_k(\mathbf{J})|^2$, with their (frequency-dependent) dressed analogs, $|\Lambda_k^d(\mathbf{J}; k\Omega(J))|^2$. In the dynamically hot limit, as expected, one has $|\Lambda_k^d|^2 \rightarrow |\Lambda_k|^2$. This is detailed in Appendix C, where we present a new approach to compute $|\Lambda_k^d|^2$.

The Landau equation (Eq. 10) satisfies a couple of important conservation laws. Up to prefactors, these are

$$\Gamma = \int dJ F(J, t) \quad (\text{total circulation}); \quad (11a)$$

$$L = \int dJ J F(J, t) \quad (\text{total momentum}); \quad (11b)$$

$$E = \int dJ H(J) F(J, t) \quad (\text{total energy}). \quad (11c)$$

If we define the Boltzmann entropy as

$$S(t) = - \int dJ F(J, t) \ln [F(J, t)], \quad (12)$$

that constitute our system, i.e. by the DF from Eq. (6), but is imposed from the outside, e.g., by being generated by a background distribution of point vortices exterior to our system. This allows us to prescribe the orbital frequency in a convenient manner.

the $1/N$ Landau equation satisfies an H -theorem, i.e. it drives $dS/dt \geq 0$. Finally, the thermodynamical equilibria, i.e. the Boltzmann DFs, of the form

$$F_B(J) \propto e^{-\beta H(J) + \gamma J}, \quad (13)$$

are generic steady states of the $1/N$ Landau equation, i.e. they satisfy $\partial F_B / \partial t = 0$ when inserted into Eq. (10). There is no guarantee, however, that the inhomogeneous Landau equation at order $1/N$ relaxes towards the Boltzmann distribution because of (local) kinetic blockings, as explained below.

Performing explicitly the sum over k in Eq. (10), the $1/N$ Landau equation can be rewritten as

$$\frac{\partial F(J, t)}{\partial t} = \gamma \frac{\partial}{\partial J} \left[\int dJ_1 \delta_D [\Omega(J) - \Omega(J_1)] \times |\Lambda_{\text{tot}}(J, J_1)|^2 \left(F(J_1) \frac{\partial F}{\partial J} - F(J) \frac{\partial F}{\partial J_1} \right) \right], \quad (14)$$

with

$$|\Lambda_{\text{tot}}(\mathbf{J})|^2 = 2 \sum_{k>0} k |\Lambda_k(\mathbf{J})|^2 \quad (15)$$

the total coupling coefficient. In that form, Eq. (14) involves the simple resonance condition $\delta_D[\Omega(J) - \Omega(J_1)]$.

Equation (14) can also be rewritten under the form of a Fokker–Planck equation [see, e.g. 42], via

$$\frac{\partial F(J, t)}{\partial t} = - \frac{\partial}{\partial J} \left[D_1(J) F(J) \right] + \frac{1}{2} \frac{\partial^2}{\partial J^2} \left[D_2(J) \frac{\partial F}{\partial J} \right]. \quad (16)$$

Here, D_1 [resp. D_2] is the first-order [resp. second-order] diffusion coefficient in action space. In the following, we will focus our interest only on the second-order diffusion coefficient. It generically reads

$$D_2(J) = 2\gamma \int dJ_1 \delta_D [\Omega(J) - \Omega(J_1)] |\Lambda_{\text{tot}}(J, J_1)|^2 F(J_1). \quad (17)$$

Physically, $D_2(J)$ describes the diffusion induced by stochastic potential fluctuations. For example, let us consider a zero-mass test particle, of initial action J , embedded in the present system. Then, on long timescales, the growth of the variance of the action increment for this particle, i.e. $\Delta J(T) = J(T) - J(0)$, is given by

$$D_2(J) = \lim_{T \rightarrow +\infty} \langle [\Delta J(T)]^2 \rangle / T. \quad (18)$$

Here, the ensemble average is taken over both the realisations of the background system and the initial phase of the test particle.

Coming back to Eq. (14) we note that if the frequency profile is monotonic, the condition $\Omega(J_1) = \Omega(J)$ implies $J_1 = J$ and Eq. (10) vanishes, i.e. $\partial F / \partial t = 0$. There is no relaxation through $1/N$ effects. This is a situation of global kinetic blocking at order $1/N$. We note that such a vanishing does not occur for the diffusion coefficient from

Eq. (17). In the presence of a non-monotonic frequency profile, for a given J , there may exist another $J_1 \neq J$ such that $\Omega(J_1) = \Omega(J)$. In that case, Eq. (10) does not vanish and the system can relax through $1/N$ effects. This is the case for profile (1), as visible in Fig. 2.

In that case, assuming that collective effects are negligible, we find from Eq. (14) that the relaxation time, i.e. the time for F to change by order unity, scales like

$$T_{\text{relax}} \simeq T_{\text{dyn}} N/q^2, \quad (19)$$

with respect to the total number of particles, N , and the system's active fraction, q . As a result, it is useful to introduce the rescaled relaxation rate and diffusion coefficients

$$\mathcal{R}_1(J, t) = \frac{\partial N(< J, t)/\partial t}{N/T_{\text{dyn}}} \frac{N}{q^2}, \quad (20a)$$

$$\mathcal{D}(J) = \frac{D_2(J)}{J_0^2/T_{\text{dyn}}} \frac{N}{q^2}, \quad (20b)$$

with $N(< J, t) = (2\pi/\gamma) \int_0^J dJ' F(J', t)$ the number of particles with an action smaller than J at time t . Its time derivative is given by $\partial N(< J, t)/\partial t = (2\pi/\gamma) \mathcal{F}(J, t)$, with the Landau flux $\partial F(J, t)/\partial t = \partial \mathcal{F}(J, t)/\partial J$, following Eq. (14). Here, $\mathcal{R}_1(J)$ and $\mathcal{D}(J)$ are both dimensionless quantities. More importantly, the $1/N$ Landau equation (Eq. 14) predicts that the two of them should be independent of both N and q .

B. Linear stability

Let us now ensure that we consider systems that are dynamically hot enough. As detailed in Appendix C, the strength of collective effects can be estimated via the “dielectric matrix”, $\mathbf{E}_k(\omega_R)$ for $\omega_R \in \mathbb{R}$. Then, the dressed coupling coefficients, Λ_k^d , that appear in the $1/N$ Balescu–Lenard equation when compared with the ones from the Landau equation scale typically like $\Lambda_k^d(\mathbf{J}; \omega_R) \sim \Lambda_k(\mathbf{J})/|\mathbf{E}_k(\omega_R)|$, with $|\mathbf{E}_k(\omega_R)| = \det[\mathbf{E}_k(\omega_R)]$, the determinant of the dielectric matrix. In practice, the closer $|\mathbf{E}_k(\omega_R)|$ is from unity, the weaker are collective effects. On the contrary, if $|\mathbf{E}_k(\omega_R)| = 0$, then the system supports an infinite amplification, i.e. this is a neutral mode. Importantly, since it describes collisionless response theory, we note that $|\mathbf{E}_k(\omega_R)|$ is independent of N and depends only on the active fraction, q .

In Fig. 3, we illustrate the Nyquist contour for profile (1), i.e. the curve of $\omega_R \mapsto |\mathbf{E}_k(\omega_R)|$ in the complex plane. In that figure, we observe that for $q \gtrsim 0.0010$, the system is linearly unstable since the Nyquist contour encloses the origin of the complex plane.⁷ Moreover, we find that

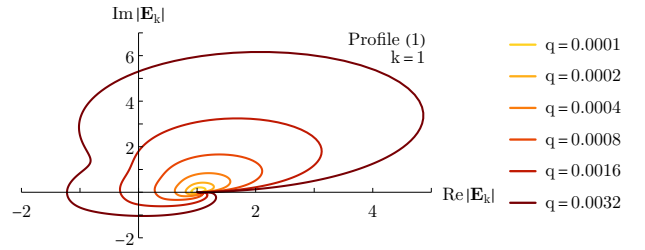


FIG. 3: Nyquist contour for profile (1) for various values of the active fraction q , for the resonance $k=1$. We refer to Appendix C for the definition of the “dielectric matrix”, $\mathbf{E}_k(\omega)$. For $q \gtrsim 0.0010$, the system is found to be linearly unstable.

for $q \lesssim 0.0003$, the contour remains close to $|\mathbf{E}_k(\omega_R)| = 1$, i.e. collective amplification is small. In all the upcoming explorations, we limit ourselves to numerical simulations with $q \leq 0.0003$, i.e. well within the range of applicability of the $1/N$ Landau equation in which collective effects are neglected.

C. Small-scale contributions

Before comparing quantitatively the kinetic prediction with N -body simulations, let us consider the contributions from small scales in Eq. (10). Indeed, that equation involves an infinite sum over the resonance numbers k , so that one should ensure that the limit $k \rightarrow +\infty$ is meaningful.

Following Eq. (15), we can naturally decompose the relaxation rate and diffusion coefficient from Eq. (20) as

$$\mathcal{R}_1(J) = \sum_{k>0} \mathcal{R}_1(J, k), \quad (21a)$$

$$\mathcal{D}(J) = \sum_{k>0} \mathcal{D}(J, k), \quad (21b)$$

where we dropped the dependence with respect to t to shorten the notations. In Fig. 4, we illustrate the dependence with k of $\mathcal{R}_1(J, k)$ and $\mathcal{D}(J, k)$, when evaluated in $J = 1.1 J_0$. We emphasise that the considered action satisfies a non-local resonance condition (Fig. 2).

From Fig. 4, we can make three observations. (i) For k small enough, one finds $\mathcal{R}_1(J, k), \mathcal{D}(J, k) \propto k^{-1}$, in agreement with the decay rate of the coupling coefficient, $k \mapsto U_k(J, J_1)$, that can directly be inferred from Eq. (B3b), as detailed in Appendix D. (ii) As k increases, we find that $k \mapsto \mathcal{R}_1(J, k)$ decreases faster than k^{-1} . This comes from the fact that for k large enough,

homogeneous systems with long-range interactions. The possibly unstable profile (1) looks similar to the “gravity” case (compare Fig. 3 with fig. 2 of [47]), while the always stable profile (2) looks similar to the “plasma” case (compare Fig. 11 with fig. 21 of [47]).

⁷ See, e.g., [47] for a simple illustration of the Nyquist method in

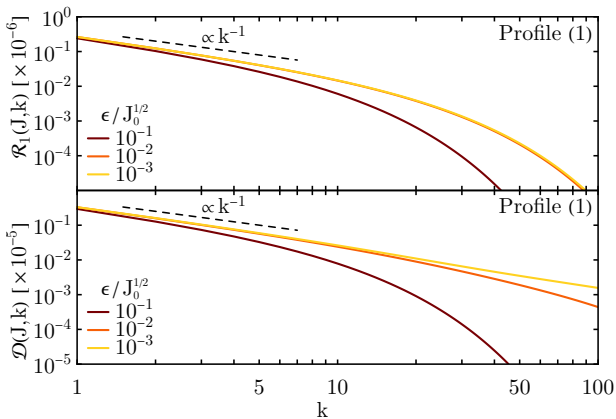


FIG. 4: Contribution to the relaxation rate, $\mathcal{R}_1(J, k)$ (Eq. 21a, top panel), and diffusion coefficient, $\mathcal{D}(J, k)$ (Eq. 21b, bottom panel), evaluated in $J/J_0 = 1.1$, as a function of the resonance number, k . The different colours correspond to different values of the softening length, ϵ . For small k , we recover the expected scaling in k^{-1} , before it being damped by softening.

the difference between the two actions, J and J_1 , that are in resonance in Eq. (14) leads to a decay faster than algebraic (see Eq. B3b). Indeed, following Eq. (B3b), and assuming $J_1 \leq J$, we find $U_k(J, J_1) \propto (J_1/J)^k / |k|$, hence driving an exponentially fast decay. (iii) On the contrary, as k increases, $k \mapsto \mathcal{D}(J, k)$ continues to scale like k^{-1} . This is because local resonances, i.e. $J_1 = J$ in Eq. (17), always contribute to the diffusion coefficient. Indeed, following Eq. (B3b), for local resonances, one finds $U_k(J, J) \propto 1/|k|$. (iv) Finally, as one increases the softening length, ϵ (Eq. 4), the decay rate with respect to k gets faster, for both the relaxation rate and the diffusion coefficient. Indeed, even when evaluated for local resonances, Eq. (B5b) roughly gives the scaling $U_k(J, J) \propto (1 - \epsilon/J)^k / |k|$, hence imposing an exponentially fast decay. This makes perfect sense physically, since softening naturally washes out contributions from small scales.

Overall, in the present regime, the $1/N$ Landau diffusion coefficient without softening suffers from a small-scale logarithmic divergence. This is similar to the Coulomb logarithm that plagues the $1/N$ Landau equation when applied to $3D$ self-gravitating systems [see, e.g. 43]. In the presence of softening, this small-scale divergence of $\mathcal{D}(J, k)$ is naturally washed out. By contrast, the $1/N$ Landau flux, because it is unaffected by local resonances, does not suffer from any small-scale divergence, even without softening. We also refer to Appendix H for a discussion of how resonance broadening also cures this small-scale divergence. In practice, in all the upcoming simulations, we will consider dynamics driven by the softened interaction potential from Eq. (4), fixing the softening length to $\epsilon = 10^{-2} J_0$.

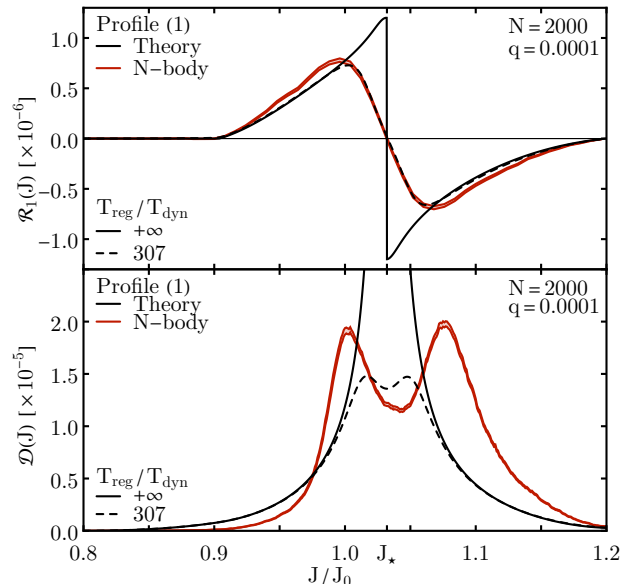


FIG. 5: Initial relaxation rate in action space, $\mathcal{R}_1(J)$ (Eq. 20a, top panel), and diffusion coefficient, $\mathcal{D}(J)$ (Eq. 20b, bottom panel), for profile (1). For the simulations, the uncertainty is illustrated with the 16% and 84% contours obtained by bootstrap over the available realisations. We refer to Appendix G for details on the numerical setup. For the prediction, the full line corresponds to the $1/N$ Landau equation (Eqs. 10 and 17), while the dashed line is from the “regularised” $1/N$ Landau equation (Eqs. 32 and 33), with the regularised time, $T_{\text{reg}}/T_{\text{dyn}} = 307$, adjusted to the slope around the sign switch of $\mathcal{R}_1(J)$. Close to the extremum of the frequency profile, broadening effects play a crucial role.

D. Relaxation and diffusion

We are now set to compare the prediction from Eq. (10) with measurements in N -body simulations. This is presented in Fig. 5, where we investigate both the relaxation rate and the diffusion coefficient. A couple of remarks can be made on Fig. 5.

1. Analytical predictions

For now, let us focus solely on the kinetic predictions, for the Landau flux (Eq. 10) in the top panel and the diffusion coefficient (Eq. 17) in the bottom panel. First, for $J/J_0 \lesssim 0.9$, it predicts $\mathcal{R}_1(J) = 0$, while, for the same range of action, one finds $\mathcal{D}(J) > 0$. Glancing back at Fig. 2, this corresponds to a range of actions, J , for which the resonance condition, $\Omega(J_1) = \Omega(J)$ (Eq. 14), imposes $J_1 = J$. As such, only local resonances are permitted by the mean frequency profile. These local resonances lead to the local vanishing of Eq. (14) because of the anti-symmetry of the collision kernel. On the contrary, such local resonances always contribute to the diffusion coefficient. As a result, the diffusion coefficient is non-zero

over the whole action domain considered. At order $1/N$, because its overall relaxation rate vanishes, the action region, $J/J_0 \lesssim 0.9$ does not relax towards the Boltzmann distribution. This is a local kinetic blocking. As such, to relax towards the statistical equilibrium state, $1/N^2$ effects must be taken into account. This will be studied in Section IV for a purely monotonic frequency profile.

Then, in Fig. 5, for $J \rightarrow J_* \simeq 1.03 J_0$, we find that the kinetic prediction for $\mathcal{R}_1(J)$ abruptly changes sign, while the prediction for $\mathcal{D}(J)$ diverges locally. This is due to the extremum of the frequency profile in $J = J_*$, as visible in Fig. 2. Let us now detail the origin of such a behaviour.

For $J \rightarrow J_*$, we may, up to a constant, approximate the frequency profile with the quadratic dependence $\Omega(J) \simeq (J - J_*)^2$, see Fig. 2. As a result, when evaluated in $J = J_* + \varepsilon$, Eqs. (14) and (17) predict for the relaxation rate and diffusion coefficient a behaviour of the form

$$\mathcal{R}_1(J_* + \varepsilon) \propto \int dJ_1 \delta_D[\varepsilon^2 - (J_1 - J_*)^2] \times [F'(J_* + \varepsilon)F(J_1) - F(J_* + \varepsilon)F'(J_1)], \quad (22a)$$

$$\mathcal{D}(J_* + \varepsilon) \propto \int dJ_1 \delta_D[\varepsilon^2 - (J_1 - J_*)^2] F(J_1). \quad (22b)$$

where we used the notation $F'(J) = \partial F / \partial J$, and dropped the coupling coefficient, $|\Lambda_{\text{tot}}|^2$, taking it to be constant.

To perform the integral over action space, we use the generic relation

$$\delta_D[f(J)] = \sum_{J_r} \delta_D[J - J_r] / |\Omega'(J_r)|, \quad (23)$$

where the sum runs over the resonant actions, J_r , such that $f(J_r) = 0$. In the present case, the resonance condition from Eq. (22) imposes $J_1 = J_* \pm \varepsilon$. As previously argued, we find that the contribution from the local resonance $J_1 = J_* + \varepsilon = J$ does not contribute to the flux, $\mathcal{R}_1(J)$, while it contributes to the diffusion coefficient, $\mathcal{D}(J)$. The non-local resonance $J_1 = J_* - \varepsilon$ contributes to both quantities. Equation (22) becomes

$$\mathcal{R}_1(J_* + \varepsilon) \propto \frac{1}{|\varepsilon|} [F'(J_* + \varepsilon)F(J_* - \varepsilon) - F(J_* + \varepsilon)F'(J_* - \varepsilon)], \quad (24a)$$

$$\mathcal{D}(J_* + \varepsilon) \propto \frac{1}{|\varepsilon|} [F(J_* + \varepsilon) + F(J_* - \varepsilon)]. \quad (24b)$$

In the limit $\varepsilon \rightarrow 0$, i.e. as one nears the extremum of the frequency profile, one finds the asymptotic behaviours

$$\mathcal{R}_1(J_* + \varepsilon) \simeq \text{Sign}[\varepsilon] \quad \text{for } \varepsilon \rightarrow 0, \quad (25a)$$

$$\mathcal{D}(J_* + \varepsilon) \simeq \frac{1}{|\varepsilon|} \quad \text{for } \varepsilon \rightarrow 0. \quad (25b)$$

As such, as visible in Fig. (5), the $1/N$ Landau equation predicts that (i) the flux in action space is discontinuous near the extremum of the frequency profile, but suffers from no divergence there; (ii) the diffusion coefficient in action space suffers from a genuine local divergence.

2. Numerical measurements

We can now compare the predictions of the flux and diffusion coefficients with measurements in N -body simulations. First, for the flux (top panel of Fig. 5), we recover that for $J/J_0 \lesssim 0.9$, relaxation is greatly delayed. This is the imprint of the local kinetic blocking. Second, as one considers larger action, say $0.9 \lesssim J/J_0 \lesssim 1.0$, we find a good agreement between the numerical simulations and the kinetic prediction, for both the flux and the diffusion coefficient. However, as J nears J_* , the location of the extremum of the frequency profile, we find that the kinetic prediction overestimates the numerical measurements. Indeed, the simulations do not exhibit the discontinuity of the flux nor the divergence of the diffusion coefficient, predicted by the $1/N$ Landau equation. In particular, the numerically-measured flux, $\mathcal{R}_1(J)$, exhibits a rather smooth change of sign, while the numerically-measured diffusion coefficient, $\mathcal{D}(J)$, presents a two-hump shape that only reaches some finite amplitude. Finally, further out in action space, i.e. for $J/J_0 \gtrsim 1.1$, we find that the kinetic prediction for the flux matches with the N -body simulations, while for the diffusion coefficient, some mismatch between the two remains. We note that this domain corresponds to actions, J , whose orbital frequency, $\Omega(J)$, is still close to the extremum one, $\Omega(J_*)$.

The mismatch observed in Fig. 5 is to be attributed to the limitations of some of the hypotheses made in the derivation of the $1/N$ Landau equation. In Fig. 5, we present a prediction with a ‘‘regularised’’ Landau equation. It offers a much more satisfactory agreement with the numerical simulations. For the diffusion coefficient, the match is improved, though far from ideal. Nonetheless, this heuristic theory still manages to reproduce the smooth change of sign of the flux and the two-hump structure of the diffusion coefficient. The exploration of such ‘‘regularised’’ kinetic predictions is the topic of Section III E.

3. Comparison with other 1D systems

Naturally, one could wonder which specific features of the current setup make it more akin to such discontinuities and the need for regularisation. Indeed, it was shown for 1D gravity [48] and the Hamiltonian Mean Field model (HMF) model [49] that the $1/N$ Landau equation can provide an excellent description of 1D relaxation processes. We briefly review here some of the key differences between these systems.

In the case of 1D gravity, there is no divergence on small-scale of the kinetic prediction [see, e.g., eq. (A7) in 48]. In addition, the frequency profile of a typical stable quasistationary state exhibits no extremum [see fig. 1 in 48]. Physically, this means that the contribution from phase mixing never vanishes, so that there is always a non-zero shear in action space. For these two reasons, the $1/N$ Landau equation produces no local discontinu-

ities or divergences in action space. For that system, one finds then an excellent match between the $1/N$ kinetic prediction and numerical measurements, both for the diffusion coefficient [see fig. 2 in 48] and the relaxation rate [see fig. 3 in 48].

Let us now consider the case of the HMF model [50]. Since the pairwise interaction in that system involves only the $k = \pm 1$ large-scale harmonics, the $1/N$ Landau equation does not suffer from any divergence on small scales. In the limit of a homogeneous quasistationary state, i.e. $F = F(v)$, the system's action is $J \sim v$, and the frequency profile is simply $\Omega(J) \sim \partial_v [\frac{1}{2}v^2] \sim v$, making it strictly monotonic. In the homogeneous limit, the HMF model is therefore submitted to a global kinetic blocking of its $1/N$ dynamics, similarly to profile (2) here. In that case, the overall relaxation is driven only by $1/N^2$ effects [51]. In the limit of weak collective amplification, the $1/N^2$ Landau equation offers a convincing match with the numerical measurements [see fig. 2 in 39].

Finally, let us consider the case of the HMF model when in an inhomogeneous, i.e. magnetised, quasistationary state. Here again, there is no divergence on small scales of the $1/N$ kinetic theory. The typical frequency profile of such a system exhibits two striking features [see, e.g., fig. 3 in 49]: (i) For $J \rightarrow 0$, i.e. in the centre of the trapped region, one has $\Omega'(J) \rightarrow 0$; (ii) For $J \rightarrow J_{\text{sep}}$, i.e. at the system's separatrix, one has $|\Omega'(J)| \rightarrow +\infty$.

Naively, one could fear that the vanishing of the frequency gradient in the system's centre would lead to the same asymptotic behaviour as in Eq. (25). In practice, for the inhomogeneous HMF model, one finds that the pairwise coupling coefficient satisfies $\lim_{J \rightarrow 0} U_k(J, J) = 0$ [see eqs. (45) and (46) in 49]. Physically, this makes sense since orbits in the system's centre correspond to particles that are exactly at rest. As a result, the Fourier transform in angle of the interaction potential between two such orbits therefore vanishes [see eq. (44) in 49]. This differs greatly from the present case of point vortices where, at the extremum of the frequency profile, one finds that $\lim_{J \rightarrow J_*} U_k(J, J)$ is non-zero. Because of the vanishing of the pairwise coupling coefficient in the centre of the inhomogeneous HMF model, one finds that both the relaxation rate and the diffusion coefficient vanish there. Therefore, the associated $1/N$ kinetic prediction exhibits no discontinuities nor divergences, and matches with numerical measurements [see, e.g., fig. 6 in 49].

At the location of the HMF separatrix, we note that the gradient of the frequency profile tends to infinity. Physically, this means that close the separatrix, pairwise resonances are swept extremely fast, rather than extremely slow as is the case close to a vanishing frequency gradient. As such, the type of discontinuities and divergences emphasised in Eq. (25) are not to be expected close to the HMF separatrix. Nonetheless, we note that this rapidly varying frequency profile leads to localised, but finite, “spikes” in the prediction for the Landau diffusion coefficient. These are clearly visible in fig. 2 of [52]

and are in agreement there with N -body measurements. Finally, we point out that the non-monotonicity of the frequency profile of the inhomogeneous HMF model is essential to prevent this system from suffering from a global kinetic blocking. Indeed, it is the non-local resonant couplings between particles located on each side of the separatrix that are solely responsible for driving the overall $1/N$ relaxation.

E. Resonance broadening

The $1/N$ Landau equation (Eq. 14) involves the sharp resonance condition, $\delta_D[\Omega(J) - \Omega(J_1)]$. Mathematically speaking, this sharp resonant Dirac comes from the fact that the derivation of the Landau equation requires the propagation of the dynamics of the DF's fluctuations, at linear order, up to infinite dynamical times [see, e.g., 42]. Yet, as a result of nonlinearities and diffusion, such an assumption is only partially true. This effect can be responsible in particular for “resonance broadening” [see, e.g. 53], as we will now explore, in a heuristic fashion.

1. Heuristic regularisation of the Landau equation

Typically, the derivation of the Landau equation starts with the introduction of the system's empirical DF, $F_d = \sum_i \gamma_i \delta_D[\mathbf{r} - \mathbf{r}_i(t)]$. This DF evolves according to the Klimontovich equation, $\partial_t F_d + [F_d, H_d] = 0$, with $H_d = H_d[F_d]$ the system's (specific) empirical Hamiltonian, and $[\cdot, \cdot]$ the Poisson bracket [42]. The empirical DF is then expanded into $F_d = F + \delta F$, with F the (smooth) ensemble-averaged DF from Section II C, and δF its fluctuations. The crucial step of the quasilinear assumption is to assume that the dynamics of δF can be expanded at linear order, to become

$$\frac{\partial \delta F}{\partial t} + [\delta F, H] + [F, \delta H] = 0, \quad (26)$$

with H the system's mean Hamiltonian, and $\delta H = \delta H[\delta F]$ the fluctuations in the Hamiltonian generated by δF . When considered within angle-action coordinates, Eq. (26) is straightforward to solve and gives a solution of the form

$$\delta F_k(J, t) \propto \delta F_k(J, 0) e^{-ik\Omega(J)t}, \quad (27)$$

with δF_k the Fourier transform in angle of δF , for the harmonic k . Physically, this solution assumes that the DF fluctuations follow the system's unperturbed mean field orbits. Finally, by sending the dynamical time to infinity, we find that

$$\text{Re} \left[\lim_{T \rightarrow +\infty} \int_0^T dt e^{-i\omega_R t} \right] \simeq \pi \delta_D(\omega_R), \quad (28)$$

with $\omega_R = \Omega(J) - \Omega(J_1)$ the resonance frequency. Therefore, in Eq. (28), we recover, heuristically, the sharp resonance condition from Eq. (14). To sum up, the $1/N$

Landau equation involves a Dirac delta as a result of two assumptions (i) the DF fluctuations are propagated linearly, i.e. along the unperturbed orbits; (ii) and this holds for infinitely long dynamical times.

Yet, these two assumptions cannot hold for so long, since we neglected the contributions from the nonlinear term, $[\delta F, \delta H]$, in Eq. (26). Heuristically, let us therefore assume that Eq. (27) must be weighted down by an exponential damping factor on some “regularisation” timescale, T_{reg} . The dynamics of the DF fluctuations would become

$$\delta F_k(J, t) \propto \delta F_k(J, 0) e^{-ik\Omega(J)t} e^{-kt/T_{\text{reg}}}. \quad (29)$$

Physically, this means that after a time T_{reg}/k , fluctuations on scale k are scattered away from their mean field orbit. This prevents the further build up of resonant interactions. Performing the same integral as in Eq. (28), we obtain

$$\text{Re} \left[\lim_{T \rightarrow +\infty} \int_0^T dt e^{-i\omega_R t} e^{-t/T_{\text{reg}}} \right] \simeq \pi \delta_{T_{\text{reg}}}(\omega_R), \quad (30)$$

where we introduced the Lorentzian

$$\delta_{T_{\text{reg}}}(\omega) = \frac{1}{\pi} \frac{T_{\text{reg}}}{1 + (\omega T_{\text{reg}})^2}. \quad (31)$$

Naturally, in the limit $T_{\text{reg}} \rightarrow +\infty$, one has $\delta_{T_{\text{reg}}}(\omega) \rightarrow \delta_D(\omega)$, hence recovering a sharp resonance condition. We refer to Appendix I1 for an alternative approach to justify the appearance of the broadened Dirac from Eq. (31) by taking into account the stochasticity of the particles trajectories.

Armed with this regularised resonance condition, we can then, heuristically, introduce “resonance broadening” in Eq. (14) by replacing its Dirac delta with this broadened condition. It becomes

$$\begin{aligned} \frac{\partial F(J, t)}{\partial t} &= \gamma \frac{\partial}{\partial J} \left[\int dJ_1 \delta_{T_{\text{reg}}}[\Omega(J) - \Omega(J_1)] \right. \\ &\quad \left. \times |\Lambda_{\text{tot}}(J, J_1)|^2 \left(F(J_1) \frac{\partial F}{\partial J} - F(J) \frac{\partial F}{\partial J_1} \right) \right]. \end{aligned} \quad (32)$$

Similarly, following the same line of thought, the diffusion coefficient from Eq. (17) can be regularised into

$$D_2(J) = 2\gamma \int dJ_1 \delta_{T_{\text{reg}}}[\Omega(J) - \Omega(J_1)] |\Lambda_{\text{tot}}(J, J_1)|^2 F(J_1). \quad (33)$$

As a side note, we point out that the broadened Dirac in Eq. (31) is always positive. This ensures that the regularised diffusion coefficient from Eq. (33) is always positive. This is an important requirement to comply with the physical definition of the diffusion coefficient from Eq. (18). Of course, we stress that Eqs. (32) and (33) are only heuristic expressions. Surely, they would deserve further theoretical developments. For example, Eq. (32) does not conserve the total energy, contrary to Eq. (14). Some additional properties of the regularised Landau

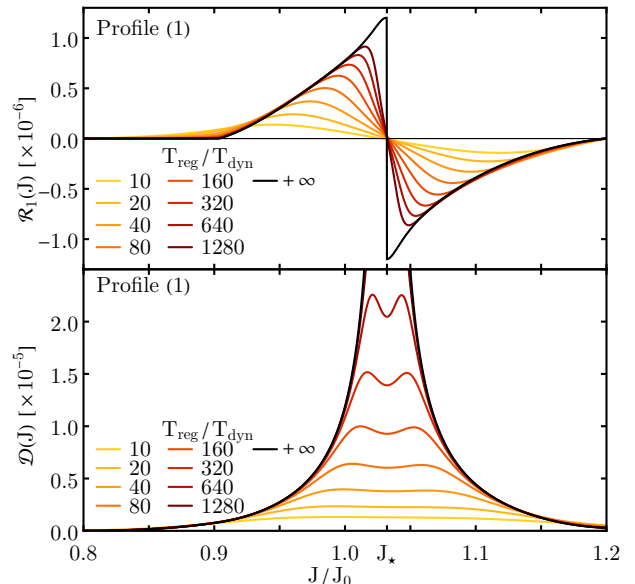


FIG. 6: Predicted initial regularised relaxation rate (Eq. 32, top panel) and diffusion coefficient (Eq. 33, bottom panel), for profile (1), as one varies the regularisation time T_{reg} , using the same convention as in Fig. 5. For $T_{\text{reg}} \rightarrow +\infty$, one recovers the $1/N$ Landau prediction from Eqs. (14) and (17).

equation (Eq. 32) are also discussed in Appendix H, in particular how it regularises both the generic divergence of the diffusion coefficient on small scales (Appendix H 1), and the divergence of the diffusion coefficient at the extremum of the frequency profile (Appendix H 2).

In Fig. 6, we compute the regularised relaxation rate and diffusion coefficients predicted by Eqs. (32) and (33), as one varies the regularisation timescale, T_{reg} . In that figure, we find that broadening effects smooth out the discontinuity and local divergence predicted by the $1/N$ Landau equation (Eq. 14) close to the extremum of the frequency profile. Reassuringly, we also find that as $T_{\text{reg}} \rightarrow +\infty$, the regularised prediction converges to the (sharp) Landau prediction. As such, varying T_{reg} in Eq. (32) allows for a smooth transition between the usual $1/N$ Landau equation and the nonlinear regime of resonance broadening. In Appendices H and I, we discuss this connexion further. In particular, we link our result with the ones obtained in previous literature in the regime of sheared and unshaped flows.

2. Finite-time diffusion coefficients

In order to visualise the appearance of resonance broadening in the simulations, taking inspiration from Eq. (18), let us introduce the finite-time diffusion coefficient as

$$D_2(J, T) = \frac{\langle [\Delta J(T)]^2 \rangle}{T}. \quad (34)$$

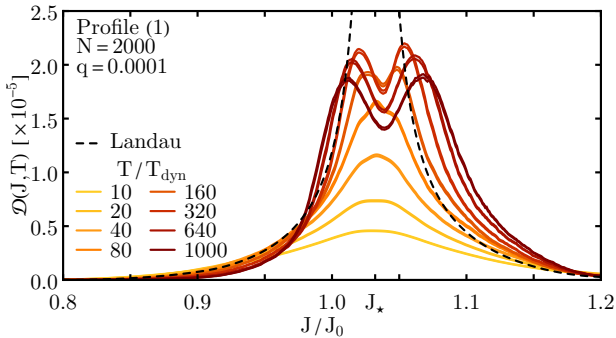


FIG. 7: Illustration of the finite-time diffusion coefficient, $\mathcal{D}(J, T)$ (Eq. 34), as measured in N -body simulations for various finite times T , for profile (1). The dashed line is the $1/N$ Landau prediction from Eq. (17). We refer to Appendix G for details on the numerical setup. As T increases, the finite-time diffusion coefficient grows, but eventually saturates to some finite amplitude, as a result of resonance broadening.

In practice, the $1/N$ Landau equation predicts that $\lim_{T \rightarrow +\infty} D_2(J, T) = D_2(J)$, with the Landau diffusion coefficient given by Eq. (17). Deviations from this limit are therefore to be attributed to nonlinear contributions spoiling some of the underlying assumptions of the $1/N$ Landau equation. Naturally, from $D_2(J, T)$, one can follow Eq. (20b) and readily define the associated rescaled finite-time diffusion coefficient, $\mathcal{D}(J, T)$.

In Fig. 7, we present numerical measurements of the finite-time diffusion coefficients, $\mathcal{D}(J, T)$, for various times T . In that figure, we note that, as one increases T , the finite-time diffusion coefficients start by following more and more closely the $1/N$ Landau diffusion coefficient. Yet, for $T/T_{\text{dyn}} \gtrsim 320$, i.e. a timescale similar to the value of T_{reg} introduced in Fig. 5, we note that (i) the growth of $\mathcal{D}(J, T)$ halts; (ii) it starts to exhibit a two-hump structure reminiscent of the one of the regularised prediction from Fig. 6. As one pushes T further, the numerically-measured finite-time diffusion coefficients even start to decay. This is because for such long time separations, the test particles have now entered their “diffusive” regime, i.e. $T \rightarrow \mathcal{D}(J, T)$ growing linearly in time, as illustrated numerically in Fig. 18 of Appendix G. In addition, we note that the mismatch between the finite-time diffusion coefficient and the $1/N$ Landau prediction is the strongest for $J \geq J_*$ rather than for $J \leq J_*$. This is because particles with $J \geq J_*$ are the ones with an orbital frequency, $\Omega(J)$, closer to the extremum frequency, $\Omega(J_*)$, as visible in Fig. 2. Overall, we argue that two-hump structure in Fig. 7 along with the saturation to finite amplitude are numerical testimonies that resonance broadening effects close to the extremum of the frequency profile play an instrumental role in the relaxation of this system.

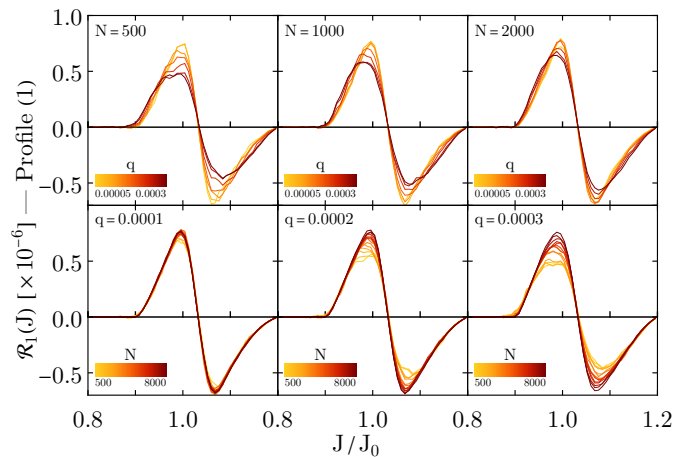


FIG. 8: Relaxation rate for profile (1), using the same convention as in Fig. 5, as one varies q for fixed N (top), or varies N for fixed q (bottom). Here, we represent only the median value over the available realisations. As one increases N and decreases q , the relaxation rate increases, but only up to some saturation.

3. Numerical comparison

Armed with a regularised kinetic equation (Eq. 32), we may use it to compare with N -body simulations. This is first presented in Fig. 5, where we adjusted the considered T_{reg} to match the slope of the numerical simulations, near the frequency extremum (Appendix D). Interestingly, we find that Eq. (32), although heuristic, offers a satisfactory match with the numerical measurements, over the whole action domain. This highlights the fact that nonlinear broadening effects are likely responsible for the effective smoothing of the relaxation rate near the extremum of the orbital frequency. We point out that, here, T_{reg} was adjusted only to match the central slope of the relaxation rate in the top panel of Fig. 5. We then used the exact same regularisation time in the bottom panel of Fig. 5 for the diffusion coefficient. There, we find that the agreement between the numerical measurement and the heuristic prediction is less convincing. Obtaining a better match requires the development of a much more involved kinetic prediction, possibly through renormalisation techniques [see, e.g., 54, and references therein]. This will be the topic of future work.

In practice, in Fig. 5, we presented a single value of (N, q) . Let us now explore the dependence of this broadening as one varies the total number of particles, N , and the system’s active fraction, q . In Fig. 8, we explore the dependence of the relaxation rate, $\mathcal{R}_1(J)$, as one varies N and q . First, in that figure, following the rescaling from Eq. (20a), we find that the dependence with respect to (N, q) is only very mild. This emphasises that, indeed, $1/N$ effects are responsible for this system’s relaxation. Yet, as one increases N and/or lowers q , one can tentatively note some increase in the overall amplitude of

the measured relaxation rate. However, this increase is only limited and ultimately saturates. As such, even if one keeps increasing N and/or lowering q , the relaxation rate, $\mathcal{R}_1(J)$, saturates and stops converging further toward the discontinuous prediction from the $1/N$ Landau equation (see Fig. 5).

4. Nonlinear timescale

Let us now be more specific on this (tentative) saturation effect. For a given value of (N, q) , let us therefore estimate the system's nonlinear timescale, T_{nl} . This time would then be the appropriate regularisation timescale, T_{reg} , to be considered in Eq. (32) when comparing with numerical simulations. Heuristically, the nonlinear time, T_{nl} , corresponds to the duration during which the quasilinear assumption from Eq. (26) holds. In that view, let us therefore equate the contribution from the nonlinear term $[\delta F, \delta H]$, with the rate of change of the DF fluctuation, $\partial_t \delta F$, in Eq. (26). We find that $|\delta F|/T_{\text{nl}} \simeq G |\delta F|^2$, where we assumed that $|\delta H| \simeq G |\delta F|$. Assuming that the statistics of the DF fluctuations is Poissonian [see, e.g., Eq. (41) in 42], we can take $|\delta F|^2 \simeq \gamma \Gamma_{\text{tot}}$, with $\gamma = \Gamma_{\text{tot}}/N$ the vortices' individual circulations, and Γ_{tot} involving the system's active fraction. Overall, we find the scaling

$$T_{\text{nl}} \simeq \frac{\sqrt{N}}{q} T_{\text{dyn}}. \quad (35)$$

Physically, the dependence of Eq. (35) makes sense. Indeed, by increasing N , i.e. by reducing the level of the Poisson fluctuations, and by lowering q , i.e. by reducing the level of collective amplification, one increases the system's nonlinear time, i.e. one allows for the quasilinear assumption to hold longer in Eq. (26).

5. Alternative view on the nonlinear timescale

Interestingly, taking inspiration from [30, 55], one can offer another heuristic derivation of the scaling of T_{nl} . Rather than being driven by nonlinearities affecting the dynamics of δF , let us assume that it is the (finite- N driven) diffusion of F that drives itself the broadening of the resonance condition in Eq. (32). This is what we explore in more detail in Appendix I recovering the regularised Landau equation from individual stochastic equations of motion. We reproduce here some of the physical insights that can be gained from this approach.

Dropping all factors of order unity, and keeping only the scaling dependence with respect to N and q , one can, heuristically, rewrite Eq. (32) as

$$\frac{\partial F}{\partial t} \propto \frac{q^3}{N} \frac{T_{\text{nl}}}{1 + (\Delta\Omega T_{\text{nl}})^2}, \quad (36)$$

where the factor q^3/N comes from $\gamma F(J)F(J_1)$ in Eq. (32), $\Delta\Omega = \Omega(J) - \Omega(J_1)$ is the resonance frequency,

and we expanded the broadened Dirac, $\delta_{T_{\text{reg}}}$, using Eq. (31) and imposing $T_{\text{nl}} = T_{\text{reg}}$. Let us then assume that it is the change in F described by Eq. (36) that is itself responsible for resonance broadening. Hence, we may make the replacement $\partial F/\partial t \rightarrow q/T_{\text{nl}}$ in Eq. (36), so that it becomes

$$\frac{1}{T_{\text{nl}}/T_{\text{dyn}}} \simeq \frac{q^2}{N} \frac{T_{\text{nl}}/T_{\text{dyn}}}{1 + (\Delta\Omega T_{\text{nl}})^2}. \quad (37)$$

Equation (37) is a self-consistent relation for the nonlinear time, T_{nl} [see, e.g., 30, 55]. This self-consistent relation is explored further in Appendix I 2 and the associated Fig. 19. Close to the extremum of the frequency profile, we may take $\Delta\Omega T_{\text{nl}} \rightarrow 0$, so that Eq. (37) gives

$$\frac{1}{(T_{\text{nl}}/T_{\text{dyn}})^2} \simeq \frac{q^2}{N}. \quad (38)$$

Ultimately, we recover the exact same scaling as in Eq. (35). Exact prefactors for this relation are obtained in Appendix I 1. Of course, it is no surprise that both approaches lead to the same scaling, since the kinetic equation is, by construction, sourced by nonlinear effects, i.e. one has $\partial F/\partial t = -\langle [\delta F, \delta H] \rangle$.

6. Numerical exploration of saturation

We can now use numerical simulations to investigate the validity of the previous heuristic interpretations, as one varies the values of (N, q) . For a given (N, q) , we can first compute the system's nonlinear time, T_{nl} , following Eq. (35). For the same parameters, we can also rely on numerical simulations to measure the system's relaxation rate, $\mathcal{R}_1(J)$. Then, just like in Fig. 5, we can adjust for the value of the regularisation time, T_{reg} (Eq. 32), to best reproduce the slope of the relaxation rate near the extremum of the frequency profile (following Fig. 15), i.e. where broadening effects play the most important role. In Fig. 9, we explore the dependence of T_{reg} as a function of T_{nl} for a large swath of values of (N, q) .

First, in Fig. 9, for small values of T_{nl} , we find that increasing T_{nl} , indeed, leads to an increase in T_{reg} . Phrased differently, in systems with strong resonance broadening, delaying the appearance of nonlinear effects leads to a more peaked relaxation rate near the frequency extremum. Unfortunately, the recovery of the expected trend $T_{\text{reg}} \propto T_{\text{nl}}$ is only tentative here. This is due, in particular, to the reduced range in T_{nl} that was considered because of the numerical complexity of simulating the present system of point vortices, for a large number of pairs (N, q) and of independent realisations (see Appendix G for details).

Second, in Fig. 9, we find that for all systems with $T_{\text{nl}} \gtrsim 3 \times 10^5 T_{\text{dyn}}$, the inferred regularisation timescale, T_{reg} , seems to saturate. Phrased differently, even if one keeps increasing the value of N and/or decreasing the value of q , the measured relaxation rate stops converging

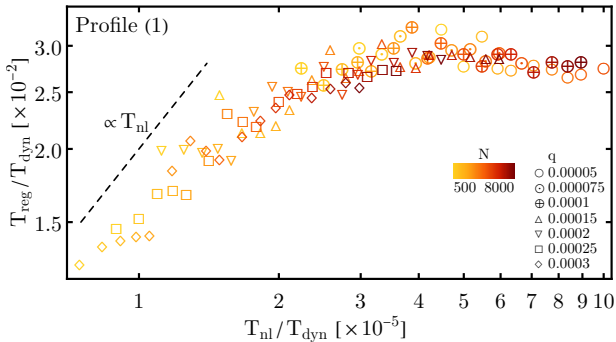


FIG. 9: Dependence of the regularisation time, T_{reg} (Eq. 32), as a function of the nonlinear time, T_{nl} (Eq. 35), using numerical simulations with different values of N (different colours) and q (different symbols). Here, T_{reg} has been obtained following Appendix D to best reproduce the relaxation rate near the frequency extremum. Surprisingly, for large values of T_{nl} , we find that T_{reg} saturates, i.e. the measured relaxation rate stops converging to the (sharp) kinetic prediction from Eq. (14).

further toward the (discontinuous) prediction from the $1/N$ Landau equation (Eq. 14). Following the numerical result from Fig. 9, this suggests that the $1/N$ Landau equation will not be recovered in the limit $N \rightarrow +\infty$. This is a very surprising result, and one for which we currently have no convincing explanation. Naturally, one could be worried that this saturation behaviour stems from some issues in the numerical simulations. To limit possible concerns, we performed a couple of convergence tests, as detailed in Appendix G. To summarize, we empirically find that

$$\frac{T_{\text{reg}}}{T_{\text{dyn}}} \simeq \begin{cases} 10^{-3} \frac{\sqrt{N}}{q} & \text{if } \frac{\sqrt{N}}{q} \lesssim 3 \times 10^5, \\ 3 \times 10^2 & \text{if } \frac{\sqrt{N}}{q} \gtrsim 3 \times 10^5. \end{cases} \quad (39)$$

Of course, the various pieces of evidence presented here only offer some glimpse on the role of nonlinear effects and resonance broadening near frequency extrema, i.e. near the breakdown of the $1/N$ Landau equation. At this stage, we can already list three possible venues to improve upon the results presented in the present section: (i) One should go beyond the heuristic regularisation of Eq. (32) to derive a self-consistent kinetic equation in that regime; (ii) One should reproduce the effect of resonance broadening in long-range interacting systems with much cheaper computations, e.g., with the quasiperiodic cube [see, e.g., 56] or with classical Heisenberg spins [see, e.g. 57]. These would be useful to check numerically the expected scaling $T_{\text{reg}} \propto T_{\text{nl}}$; (iii) Finally, leveraging the same systems, one should explore the relaxation of systems with much larger values of T_{nl} to confirm the saturation effect observed in Fig. 9. All these investigations are left for future work.

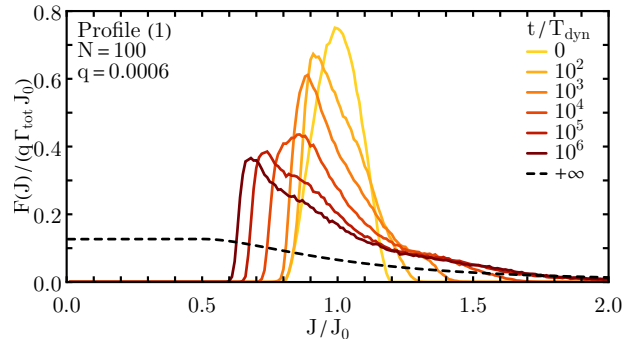


FIG. 10: Relaxation in N -body simulations of profile (1) toward the thermodynamical equilibrium (Eq. 13). Different colours correspond to different times (here the median value over the available realisations), while the dashed line is the expected Boltzmann equilibrium (see Appendix E). Relaxation is delayed by a local kinetic blocking induced by the absence of resonances in certain regions of the non-monotonic frequency profile (see Fig. 2).

F. Long-term relaxation

Ultimately, the present system relaxes toward the Boltzmann distribution (Eq. 13). And, we refer to Appendix E for details on how this equilibrium may be determined given some initial conditions.

In Fig. 10, we use N -body simulations to illustrate this long-term relaxation to the statistical equilibrium. In that figure, one can note that the relaxation of the system toward the central region is particularly slow. This follows from the particular shape of the present non-monotonic frequency profile (see Fig. 2). Indeed, particles within the system's inner regions, i.e. with small actions, cannot resonantly couple to more external regions, i.e. to particles with larger actions. This was responsible for the local kinetic blocking, already visible in the $1/N$ Landau flux from Fig. 5. As such, these inner regions cannot relax through $1/N$ effects and must wait for the outer regions to diffuse, via $1/N^2$ effects, so that non-local resonances get populated and that the more efficient $1/N$ relaxation may proceed. This lack of efficient resonant couplings is responsible for the system's particularly slow diffusion within the core regions. Phrased differently, although the system's frequency profile is non-monotonic, there still exist regions in action space that only relax, at least initially, via $1/N^2$ effects. Such next-order contributions are the focus of the upcoming section.

IV. $1/N^2$ DYNAMICS

A. Kinetic equation

We now consider profile (2), i.e. a system with a monotonic frequency profile (Fig. 2). In that case, the resonance condition in the $1/N$ Landau equation (Eq. 10)

imposes $J_1 = J$, hence leading to the vanishing of the crossed term $\mathbf{k} \cdot \partial F_2 / \partial \mathbf{J}$. This is a kinetic blocking, and there is no relaxation driven by $1/N$ effects.⁸ Relaxation is greatly hampered, and occurs only through $1/N^2$ effects. Placing themselves within this regime and neglecting collective effects, [44] derived a closed kinetic equation describing this relaxation. The inhomogeneous $1/N^2$ Landau equation reads

$$\frac{\partial F(J, t)}{\partial t} = \gamma^2 \frac{\partial}{\partial J} \left[\sum_{k_1, k_2} (k_1 + k_2) \mathcal{P} \int dJ_1 dJ_2 |\Lambda_{k_1 k_2}(\mathbf{J})|^2 \times \delta_D(\mathbf{k} \cdot \boldsymbol{\Omega}) \mathbf{k} \cdot \frac{\partial}{\partial \mathbf{J}} F_3(\mathbf{J}) \right], \quad (40)$$

with \mathcal{P} the Cauchy principal value acting on the integral over dJ_1 . We refer to Appendix F for the expression of the coupling coefficients, $|\Lambda_{k_1 k_2}(\mathbf{J})|^2$, which are independent of both N and q . In Eq. (40), we shortened the notations with the 3-vectors $\mathbf{J} = (J, J_1, J_2)$, $\boldsymbol{\Omega} = (\Omega[J], \Omega[J_1], \Omega[J_2])$, and $\mathbf{k} = (k_1 + k_2, -k_1, -k_2)$, as well as $F_3(\mathbf{J}) = F(J)F(J_1)F(J_2)$. At the present time, the generalisation of Eq. (40) that accounts for collective effects is unknown.

Just like the $1/N$ Landau equation (Eq. 10), the $1/N^2$ Landau equation (Eq. 40) conserves the total circulation, momentum and energy (Eq. 11), satisfies an H -theorem for the Boltzmann entropy (Eq. 12), and vanishes exactly for the Boltzmann DF (Eq. 13).

Equation (40) contains an intricate resonance condition, $\delta_D(\mathbf{k} \cdot \boldsymbol{\Omega})$, involving three particles. Even with a monotonic frequency profile, this resonance condition allows for non-local resonances, i.e. triplets of actions, \mathbf{J} , that are not all identical. As a result, no further kinetic blocking is generically to be expected.⁹ In that case, we find from Eq. (40) that the relaxation time scales like

$$T_{\text{relax}} \simeq T_{\text{dyn}} N^2 / q^4, \quad (41)$$

with respect to N and q , in the limit where collective effects can be neglected. As a result, it is useful to introduce the rescaled relaxation rate

$$\mathcal{R}_2(J, t) = \frac{\partial N(< J, t) / \partial t}{N / T_{\text{dyn}}} \frac{N^2}{q^4}, \quad (42)$$

using the same notation as in Eq. (20a). In that case, the $1/N^2$ Landau equation (Eq. 40) predicts that $\mathcal{R}_2(J)$ should be independent of both N and q .

⁸ Kinetic blocking at order $1/N$ also holds when accounting for collective effects, as described by the inhomogeneous Balescu-Lenard equation.

⁹ Though, we refer to [45] for the (involved) example of a bare second-order kinetic blocking for a particular class of potentials of interaction. For the potential of interaction of point vortices (Eqs. 3 and 4), there is no kinetic blocking at the order $1/N^2$ and the DF relaxes through Eq. (40) towards the Boltzmann DF.

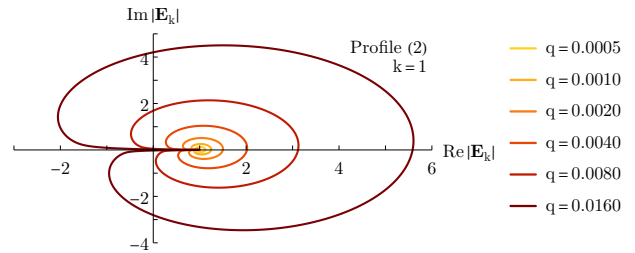


FIG. 11: Same as Fig. 3 but for profile (2). Here, for all values of q , the system is always found to be linearly stable.

B. Linear stability

The scaling from Eq. (41) only holds in the limit of weak collective amplification. Once again, we can use linear response theory to determine an appropriate range of active fraction for which collective effects are negligible. This is illustrated in Fig. 11 for profile (2) using Nyquist contours. Interestingly, in this figure, we find that the geometry of the Nyquist contours is such that, whatever the considered value of q , the contour never encloses the origin of the complex plane. Phrased differently, contrary to profile (1), here for profile (2), whatever the system's active fraction, the system's initial distribution is linearly stable. Of course, linear stability is not synonymous with weak collective amplification. Indeed, in Fig. 11, we find that for $q \gtrsim 0.004$, the Nyquist contour gets extremely close to the origin, i.e. there exist real frequencies for which the system amplifies very significantly perturbations. In practice, in all the upcoming simulations, we limit ourselves to simulations with $q \leq 0.0007$, so that Eq. (40) applies.

C. Small-scale contributions

As for the $1/N$ case, let us first focus on the contributions from small scales. Indeed, Eq. (40) involves an infinite sum over the resonance numbers (k_1, k_2) , i.e. one ought to ensure that the limits $k_1, k_2 \rightarrow +\infty$ are meaningful.

Following Eq. (40), we decompose the relaxation rate from Eq. (42) as

$$\mathcal{R}_2(J) = \sum_{k>0} \mathcal{R}_2(J, k), \quad (43)$$

where we introduced

$$\mathcal{R}_2(J, k) = \sum_{\substack{k_1, k_2 \\ \text{Max}[|k_1|, |k_2|] = k}} \mathcal{R}_2(J, k_1, k_2). \quad (44)$$

In Fig. 12, we illustrate the dependence of $k \mapsto \mathcal{R}_2(J = 1.1 J_0, k)$.

From that figure, one can make a couple of observations: (i) For k small enough, one finds $\mathcal{R}_2(J, k) \propto k^{-2}$.

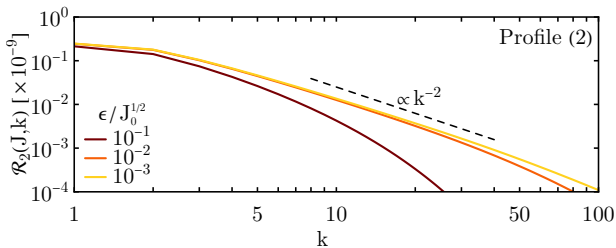


FIG. 12: Same as Fig. 4, but for the $1/N^2$ Landau equation (Eq. 40) and profile (2) (Eq. 43). For small k , i.e. scales larger than ϵ , we recover the expected scaling in k^{-2} .

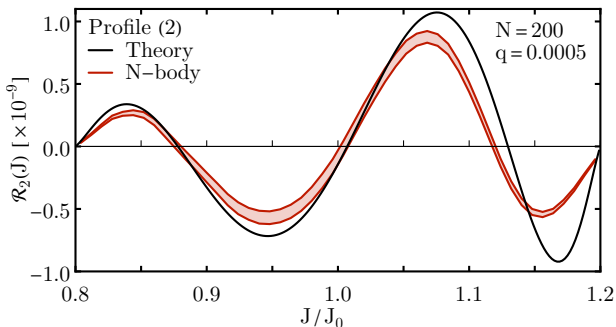


FIG. 13: Same as Fig. 5 but for profile (2). For that profile, relaxation is driven by $1/N^2$ effects (Eq. 40), and hence is much delayed. The origin of the mismatch for large actions remains unclear.

This is in agreement with the decay rate that can directly be inferred from Eq. (40), as detailed in Appendix F. (ii) As one increases the softening length, ϵ , the contribution to the relaxation rate decays faster with k . As expected, introducing softening leads to the vanishing of the contribution from small scales. Overall, we find that Eq. (40) does not suffer from any small scale divergence (even in the absence of softening), when applied to the dynamics of point vortices.

D. Relaxation rate

We are now set to compare the kinetic prediction from Eq. (40) with measurements in N -body simulations. This is presented in Fig. 13. In that figure, we find a welcome agreement between the $1/N^2$ prediction and the numerical measurements. This is one of the main result of the present work, i.e. a quantitative validation of the $1/N^2$ kinetic theory of point vortices. One should point out the presence of a mismatch for $J/J_0 \gtrsim 1.1$. Such a disagreement could stem from contributions associated with collective effects, since Eq. (40) neglects them altogether. We point out that all previous explicit applications of the $1/N^2$ kinetic equation have always uncovered a mismatch, see, in particular, fig. 2 in [39] for the HMF model, fig. 1 in [40] for the ring model, and fig. 1 in [44]

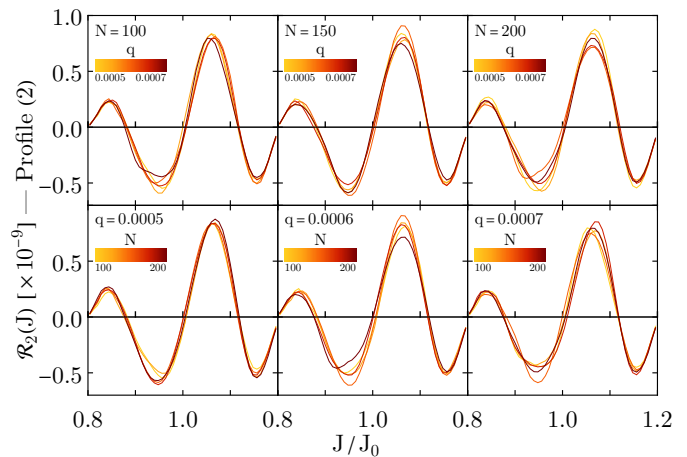


FIG. 14: Same as Fig. 14, but for profile (2). As one varies N and/or q , the (rescaled) relaxation rate, $\mathcal{R}_2(J)$ (Eq. 42), remains, in essence, unchanged.

for Heisenberg spins. A next step to clarify this effect would be to generalise Eq. (40) to the case with collective effects, i.e. to derive, for the first time, the $1/N^2$ Balescu–Lenard equation.

Building upon the previous case of profile (1), one could be worried that resonance broadening effects could be polluting the measurement from Fig. 13. In Fig. 14, we repeat the measurement of the relaxation rate, $\mathcal{R}_2(J)$, for various values of N and q . In that figure, contrary to Fig. 8, we observe no clear trend with respect to modifications of N and/or q . As a result, for the present monotonic frequency profile, there does not seem to be any clear signature from nonlinear effects that would cause a significant broadening of the three-body resonance condition from Eq. (40).

V. CONCLUSIONS

In this paper, we investigated the long-term relaxation of long-range interacting point vortices in $2D$ hydrodynamics within axisymmetric configurations. We showed how the generic kinetic theory of inhomogeneous long-range interacting systems can readily be applied to point vortices. In that context, we emphasised the existence of two regimes of relaxation: (i) if the system's mean frequency profile is non-monotonic, the distribution of point vortices relaxes through $1/N$ effects. In the limit of negligible collective amplification, this is governed by the $1/N$ inhomogeneous Landau equation (Eq. 10); (ii) if the mean frequency profile is monotonic, the system is then submitted to a kinetic blocking, which prevents $1/N$ effects from driving any relaxation. In that case, neglecting once again collective effects, the system's relaxation is described by the $1/N^2$ inhomogeneous Landau equation (Eq. 40).

For both regimes of relaxation, we reported on the

agreement between the prediction from kinetic theories and measurements in direct numerical simulations. Using these same simulations, we also recovered the expected scalings with respect to the total number of particles and the system's active fraction. Finally, we emphasised the signature of nonlinear resonance broadening near the extremum of the frequency profile.

Naturally, the present work is only one small step toward building a finer understanding of long-term relaxation. Let us conclude this work by mentioning a few possible venues for future investigations.

1/N² Balescu–Lenard equation. At order 1/N, when collective effects cannot be neglected, the Landau equation becomes the Balescu–Lenard equation [41, 42]. In the presence of a kinetic blocking, the 1/N² version of the Balescu–Lenard equation is currently unknown. Although this is no easy challenge, it would be worthwhile to derive such a generalisation, to investigate the impact of collective effects in kinetic blockings.

Resonance broadening. Of course, it would be interesting to investigate further the effect of resonance broadening unveiled in Fig. 5. On the numerical front, one could revisit this problem using N -body simulations in a simpler toy model. For example, the homogeneous Hamiltonian Mean Field model [50] with the kinetic energy, $\frac{1}{2}v^2$, changed for $\frac{1}{3}v^3$, hence ensuring a non-monotonic mean frequency profile, similar to the one from profile (1) here (see Fig. 2). Similarly, the case of classical Heisenberg spins could also prove insightful [see, e.g. 57]. On the theoretical front, going beyond the heuristic regularisation from Eq. (32) is particularly challenging, in particular to ensure the expected conservation laws and H -theorem. One possible venue could be to explore systematic methods stemming from renormalisation theory [see, e.g., 54, and references therein].

Large deviations. We focused our interest on the ensemble-averaged evolution. Going beyond the mean dynamics, one should also investigate the dispersion of independent realisations around that mean evolution. This is the promise of large deviation theory applied to kinetic equations [58, 59], though its quantitative comparison with N -body simulations remains to be done.

Marginal stability. In the presence of a monotonic frequency profile, an axisymmetric distribution of point vortices is always submitted to a kinetic blocking, independently of the strength of collective effects. Yet, as a system nears marginal stability, i.e. as the oscillation of the damped modes take longer and longer to fade away, mode-particle couplings are expected to get more and more efficient at driving the system's relaxation [see, e.g., 60, 61]. It would be interesting to investigate the impact that such “quasilinear” contributions can have on kinetic blockings.

Spectrum of circulations. Here, we considered systems with a single population of vortices, sharing all the exact same individual circulation. In the view of better understanding segregation processes, one should investigate systems with different circulations, in particular

different signs [see, e.g., 30, 37].

Acknowledgments

This work is partially supported by the grant Segal ANR-19-CE31-0017 of the French Agence Nationale de la Recherche and by the IDEX Sorbonne Université. This research was supported in part by grant NSF PHY-2309135 to the Kavli Institute for Theoretical Physics (KITP). We warmly thank S. Flores and A. El Rhirhayi for detailed remarks and suggestions. We are grateful to S. Rouberol for the smooth running of the Infinity cluster where the simulations were performed.

Appendix A: Background profiles

In this Appendix, we detail our prescription for the external potentials introduced in Eq. (9).

The mean self-consistent potential generated by the point vortices reads

$$\begin{aligned} H_\epsilon[F] &= \int d\mathbf{r}' U_\epsilon(\mathbf{r}, \mathbf{r}') F(r') \\ &= 2\pi \int dJ' U_{\epsilon, k=0}(J, J') F(J'), \end{aligned} \quad (\text{A1})$$

with $F(J')$ the DF from Eq. (6), and the Fourier-transformed (softened) interaction potential, $U_{k,\epsilon}(J, J')$ following Eq. (B4). Fortunately, this integral, as well as the associated orbital frequency, can be explicitly performed, using symbolic computing (*Mathematica*), even in the presence of softening. We implemented these expressions in the N -body simulations (see Appendix G).

For profile (1), we assume that it is generated by the background DF

$$F_b(J) = \Theta[J \geq J_b] \frac{\Gamma_{\text{tot}}^b}{\pi \sigma_b} \frac{1}{[1 + |J - J_b|/\sigma_b]^3}, \quad (\text{A2})$$

with $\Gamma_{\text{tot}}^b = \Gamma_{\text{tot}}$ the background total circulation. Here, J_b is the shift of the background DF, while σ_b is its width. Using once again Eq. (A1), one can compute explicitly the associated, unsoftened, potential. Although somewhat lengthy, this expression can be obtained using symbolic computing. In practice, in the N -body simulations, we imposed $J_b/J_0 = \frac{1}{2}$ and $\sigma_b/J_0 = 1$, for which the generated frequency profile is non-monotonic in the vicinity of the active DF, see Fig. 2.

For profile (2), we consider Eq. (A2) in the limit $J_b = 0$. In that case, the (unsoftened) mean Hamiltonian reads

$$H_0(J) = \frac{G\Gamma_{\text{tot}}^b}{4\pi} \frac{1 - (1 + J/\sigma_b) \ln[2(J + \sigma_b)]}{1 + J/\sigma_b}, \quad (\text{A3})$$

while the mean frequency is $\Omega_0(J) = \Omega_b g(J/\sigma_b)$ with the frequency scale $\Omega_b = -G\Gamma_{\text{tot}}^b/(2\pi\sigma_b)$ and the dimensionless monotonic function

$$g(x) = \frac{1 + \frac{1}{2}x}{(1+x)^2}. \quad (\text{A4})$$

Such a model is a pleasant choice as it allows for the resonance condition in Eq. (40) to be explicitly solved. Indeed, for $0 < \varpi \leq 1$, one has

$$g(x) = \varpi \implies x = \frac{1 - 4\varpi + \sqrt{1 + 8\varpi}}{4\varpi}. \quad (\text{A5})$$

This greatly eases the numerical implementation of the $1/N^2$ kinetic equation. In practice, in the N -body simulations, we imposed $\sigma_b/J_0 = 1$.

Appendix B: Interaction potential

In the absence of any softening, the pairwise interaction potential (Eq. 3) reads

$$U(\mathbf{r}, \mathbf{r}') = -\frac{G}{2\pi} \ln |\mathbf{r} - \mathbf{r}'|. \quad (\text{B1})$$

Its Fourier expansion in angle is

$$U(\mathbf{r}, \mathbf{r}') = \sum_{k=-\infty}^{+\infty} U_k(J, J') e^{ik(\theta - \theta')}, \quad (\text{B2})$$

with $U_k(J, J') = U_k(r[J], r'[J'])$ following [see eq. (A15) in 34]

$$U_0(r, r') = -\frac{G}{2\pi} \ln(r_{\max}), \quad (\text{B3a})$$

$$U_k(r, r') = \frac{G}{4\pi} \frac{1}{|k|} \left(\frac{r_{\min}}{r_{\max}} \right)^{|k|}. \quad (\text{B3b})$$

In that expression, we introduced $r_{\min} = \text{Min}[r, r']$ and $r_{\max} = \text{Max}[r, r']$. Using the relation $J = \frac{1}{2}r^2$, it is then straightforward to obtain the coupling coefficient in action space, $U_k(J, J')$.

To soften the interaction on small scales, we transform Eq. (B1) into

$$U(\mathbf{r}, \mathbf{r}') = -\frac{G}{2\pi} \ln \left([|\mathbf{r} - \mathbf{r}'|^2 + \epsilon^2]^{1/2} \right), \quad (\text{B4})$$

with ϵ some fixed softening length. Following the same approach as in appendix B of [62], the Fourier expansion from Eq. (B3) becomes

$$U_0(r, r') = -\frac{G}{2\pi} \ln(r_\alpha), \quad (\text{B5a})$$

$$U_k(r, r') = \frac{G}{4\pi} \frac{1}{|k|} \left(\frac{r_\beta}{r_\alpha} \right)^{|k|}, \quad (\text{B5b})$$

where we introduced the two radii

$$r_\alpha = \left[\frac{1}{2} \left(\left\{ ((r+r')^2 + \epsilon^2) ((r-r')^2 + \epsilon^2) \right\}^{1/2} + r^2 + r'^2 + \epsilon^2 \right) \right]^{1/2}, \quad (\text{B6a})$$

$$r_\beta = \frac{rr'}{r_\alpha}. \quad (\text{B6b})$$

Appendix C: Linear response theory

Balescu–Lenard equation. When accounting for collective effects, the inhomogeneous Landau equation (Eq. 10) becomes the inhomogeneous Balescu–Lenard (BL) equation [41, 42]. It has the exact same functional form except that the bare coupling coefficients, $U_k(J, J')$, become the (frequency-dependent) dressed ones, $U_k^d(J, J'; \omega)$, to be used in Eq. (D1).

Self-consistent relation. The dressed coupling coefficients satisfy the self-consistent relation [see, e.g., 42]

$$U_k^d(J, J'; \omega) = U_k(J, J') + 2\pi \int dJ'' \frac{k \partial F / \partial J''}{(k\Omega'' - \omega)_-} U_k(J, J'') U_k^d(J'', J; \omega), \quad (\text{C1})$$

with $\Omega'' = \Omega(J'')$. We also introduced the regularised complex Hilbert kernel [see, e.g., 63, and references therein]

$$\frac{1}{z_-} = \lim_{T \rightarrow +\infty} \frac{1 - e^{-izT}}{z}. \quad (\text{C2})$$

The dressed coupling coefficients, $U_k^d(\omega)$, capture the strength of the collective amplification in the system.

Matrix rewriting. In inhomogeneous systems, $U_k^d(\omega)$, is typically evaluated using Kalnajs' basis method [64]. Here, we resort to a simpler method that frees us from having to construct tailored basis elements, as we now detail.

First, in Eq. (C1), we note that both the resonance number, k , and the frequency, ω , are external labels of the integral over dJ'' . Let us therefore assume that we can decompose the action domain into a finite number of bins of length ΔJ . This provides us then with a list of action, $\{J_i\}_i$, around which each bin is centred. We now introduce the matrices, \mathbf{U}_k and $\mathbf{U}_k^d(\omega)$, via

$$(\mathbf{U}_k)_{ij} = U_k(J_i, J_j), \quad (\text{C3a})$$

$$(\mathbf{U}_k^d(\omega))_{ij} = U_k^d(J_i, J_j; \omega). \quad (\text{C3b})$$

Approximating the integral from Eq. (C1) with the midpoint rule, it becomes the matrix relation

$$\mathbf{U}_k^d(\omega) = \mathbf{U}_k + \mathbf{U}_k \mathbf{M}_k(\omega) \mathbf{U}_k^d(\omega), \quad (\text{C4})$$

where we introduced the diagonal matrix

$$(\mathbf{M}_k(\omega))_{ij} = \delta_{ij} 2\pi \Delta J \frac{k \partial F / \partial J_i}{(k\Omega(J_i) - \omega)_-}. \quad (\text{C5})$$

After manipulation, Eq. (C4) finally becomes

$$\mathbf{E}_k(\omega) \mathbf{U}_k^d(\omega) = \mathbf{U}(k), \quad (\text{C6})$$

or equivalently

$$\mathbf{U}_k^d(\omega) = \mathbf{E}_k(\omega)^{-1} \mathbf{U}(k), \quad (\text{C7})$$

where we introduced the “dielectric” matrix

$$\mathbf{E}_k(\omega) = \mathbf{I} - \mathbf{U}(k) \mathbf{M}_k(\omega), \quad (\text{C8})$$

with \mathbf{I} the identity matrix. Heuristically, Eq. (C6) should be interpreted as $U^d \sim U/E$, hence describing collective dressing. In particular, for a given resonance number, k , a system supports a mode at frequency ω_M if one has

$$\det[\mathbf{E}_k(\omega_M)] = 0. \quad (\text{C9})$$

Importantly, the present approach (i) does not require any potential/density basis elements; (ii) can readily be applied to softened pairwise interactions. Since the approach from this Appendix directly computes the dressed coupling coefficients, U^d , it can readily be used to predict the BL relaxation rate [41, 42]. This provides an alternative to the traditional basis method [64] used, for example, in the BL predictions of [48].

Nyquist contours. In Figs. 3 and 11, the Nyquist contours represent, in the complex plane, the values of the function $\omega_R \in \mathbb{R} \rightarrow \det[\mathbf{E}_k(\omega_R + i\eta)] = |\mathbf{E}_k(\omega_R + i\eta)|$. Phrased differently, these figures show the imaginary part of $|\mathbf{E}_k(\omega_R + i\eta)|$ as a function of its real part, as one varies ω_R . In practice, (i) we used 500 points to sample the action domain in Eq. (C3), and (ii) we regularised Eq. (C5) with the small positive imaginary part $\eta = 10^{-3} \Omega(J_0)$, so that $1/(\omega_R + i\eta)_- \rightarrow 1/(\omega_R + i\eta)$. We checked that varying the number of sampling points or the value of η had no impact on the plotted Nyquist curves.

Appendix D: $1/N$ kinetic theory

$1/N$ Landau equation. Following [42], in the absence of collective effects, the inhomogeneous Landau equation (Eq. 10) satisfies

$$|\Lambda_k(\mathbf{J})|^2 = 2\pi^2 |U_k(J, J_1)|^2, \quad (\text{D1})$$

where $U_k(J, J_1)$ is the Fourier transformed interaction potential (see Appendix B). Performing the sum over k , one readily obtains Eq. (14). For the unsoftened interaction potential, the sum can be carried out explicitly [see, e.g., appendix B in 33].

Small-scale contributions. In Fig. 4, we present the respective contribution of small scale resonances, i.e. large

k , to the $1/N$ Landau relaxation rate. Let us recover the main features of that figure directly from Eq. (10). For $J' \rightarrow J$, Eq. (B3b) gives $U_k(J, J') \simeq k^{-1}$, so that Eq. (D1) gives $|\Lambda_k(\mathbf{J})|^2 \simeq k^{-2}$. When used in Eq. (15), we find from Eq. (14) that each scale contributes like k^{-1} . In practice, this scaling of the relaxation rate only holds for k small enough, before the difference between the two resonating actions J and J_1 leads a decay faster than k^{-1} in Eq. (B3b). For the diffusion coefficient from Eq. (17), because local resonances always contribute to it, i.e. $J_1 = J$ in Eq. (17), the exact match of the two resonating actions allows for the scaling in k^{-1} to hold throughout, as visible in Eq. (B3b). This is responsible for a small-scale logarithmic divergence of the diffusion coefficient, in systems driven by the unsoftened interaction from Eq. (3) (see Appendix H). As could have been expected, increasing the considered softening length accelerates the decay of the small-scale contributions. These various trends are further discussed in Section III C and recovered in Fig. 4.

Computing the kinetic prediction. In practice, to evaluate Eq. (14), one invokes the relation

$$\delta_D[\Omega(J) - \Omega(J_1)] = \sum_{J_r} \frac{\delta_D(J - J_r)}{|d\Omega/dJ_r|}, \quad (\text{D2})$$

where the J_r satisfy $\Omega(J_r) = \Omega(J)$. Used in Eq. (14), we get

$$\frac{\partial F(J, t)}{\partial t} = \gamma \frac{\partial}{\partial J} \left[\sum_{J_r} \frac{|\Lambda_{\text{tot}}(J, J_r)|^2}{|d\Omega/dJ_r|} \times \left(F(J_r) \frac{\partial F}{\partial J} - F(J) \frac{\partial F}{\partial J_r} \right) \right]. \quad (\text{D3})$$

We implemented this expression to obtain Fig. 5, limiting the sum over k in Eq. (15) to $|k| \leq 100$. We used the same approach to compute the $1/N$ Landau diffusion coefficient from Eq. (17).

Computing the regularised prediction. To compute prediction from the “regularised” $1/N$ Landau equation (Eq. 32), we evaluated the integral over dJ_1 therein using a simple midpoint rule with 1000 nodes within the interval $J_0 - \sigma_0 \leq J_1 \leq J_0 + \sigma_0$, limiting, once again, the sum over k in Eq. (15) to $|k| \leq 100$. We proceeded similarly to evaluate the regularised diffusion coefficient from Eq. (33).

Inferring the regularisation time. In Fig. 9, we compare the value of the nonlinear time, T_{nl} (Eq. 35), with the regularisation time, T_{reg} , inferred from N -body simulations. To obtain this figure, we proceeded as follows. First, we computed the regularised relaxation rate from Eq. (32) for $T_{\text{reg}}/T_{\text{dyn}} = 10 \times 2^n$ with $0 \leq n \leq 7$. Then, for each such prediction, we performed a linear fit of the relaxation rate within the domain $1.022 \leq J/J_0 \leq 1.042$, the action domain centred around the change of sign of the relaxation rate. These measurements are presented in Fig. 15. In that figure, we find a simple power-law dependence linking the regularisation time, T_{reg} , with the central slope of the relaxation rate as a function of the

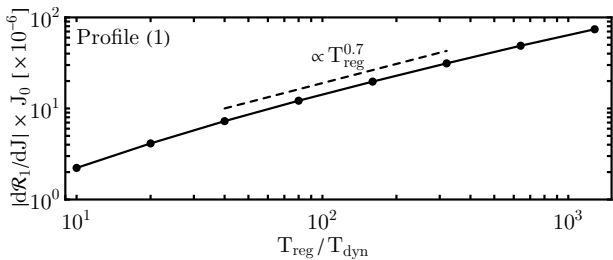


FIG. 15: Dependence of the predicted central slope of the relaxation rate with respect to the action (see, e.g., Fig. 6), as a function of the regularisation time, T_{reg} , used in Eq. (32).

action. Finally, we used the measurements from Eq. (15) to infer the “best” regularisation time presented in Fig. 9.

Appendix E: Boltzmann equilibrium

The present systems have three global invariants. Following Eq. (11), these are (i) the total circulation Γ ; (ii) the total momentum L ; and (iii) the total energy E . In practice, since we consider systems with small active fraction, q , for simplicity, we may approximate the total energy by limiting ourselves only to the axisymmetric external potential, H_0 , introduced in Eq. (9). Doing so, we neglect the “self-gravitating” contribution from the particles’ pairwise couplings, and the total energy (Eq. 11c) simply becomes $E = \int dJ H_0(J) F(J, t)$.

As a result of these conservations, the associated Boltzmann equilibria generically read (Eq. 13)

$$F_B(J) = \alpha e^{-\beta H_0(J) + \gamma J}, \quad (\text{E1})$$

where $(\alpha, \beta, \gamma) = \mathbf{X}$ are three parameters to be found to comply with the conservation of $(\Gamma, L, E) = \mathbf{Y}$. Phrased differently, given some initial DF, $F_0 = F(t=0)$, the associated long-term thermodynamical Boltzmann equilibrium is specified by the set of parameters, \mathbf{X} , such that $\mathbf{Y}[F_B(\mathbf{X})] = \mathbf{Y}[F_0]$.

Such a self-consistent relation can be solved using Newton’s algorithm. Given some guess $\mathbf{X}^{(n)}$, we perform the iteration

$$\mathbf{X}^{(n+1)} = \mathbf{X}^{(n)} - \mathbf{J}^{-1}[\mathbf{X}^{(n)}] (\mathbf{Y}[\mathbf{X}^{(n)}] - \mathbf{Y}_0), \quad (\text{E2})$$

with $\mathbf{Y}_0 = \mathbf{Y}[F_0]$. In that expression, we also introduced the Jacobian matrix

$$(\mathbf{J}[\mathbf{X}])_{ij} = \frac{\partial Y_i[\mathbf{X}]}{\partial X_j}. \quad (\text{E3})$$

One can then iterate Eq. (E2) up to convergence, i.e. up to $\max_i |X_i^{(n+1)} - X_i^{(n)}| \leq \epsilon$, with, here, $\epsilon = 10^{-12}$.

To obtain the Boltzmann DF represented in Fig. 10, we computed numerically the integrals defining the invariants \mathbf{Y} (Eq. 11) as well as the Jacobian \mathbf{J}

(Eq. E3) using the midpoint rule with 10^5 nodes within the range $0 \leq J/J_0 \leq 10^3$. The initial guess was fixed to $\mathbf{X}^{(0)} = [q\Gamma_{\text{tot}}^b/(2\pi), 0, 0]$. Convergence was reached in 20 iterations, leading to the final value $\mathbf{X}^{(+\infty)} \simeq [8.88 \times 10^{-4}/\Gamma_{\text{tot}}^b, -40.0/(G\Gamma_{\text{tot}}^b), 6.26 \times 10^{-3}/J_0]$.

Appendix F: $1/N^2$ kinetic theory

$1/N^2$ Landau equation. Following [44], the coupling coefficients of the inhomogeneous $1/N^2$ Landau equation read

$$|\Lambda_{k_1 k_2}(\mathbf{J})|^2 = 2\pi^3 \left| \frac{[\Omega(J) - \Omega(J_1)] \mathcal{U}_{k_1 k_2}^{(1)}(\mathbf{J}) + k_2 \mathcal{U}_{k_1 k_2}^{(2)}(\mathbf{J})}{k_1(k_1 + k_2) [\Omega(J) - \Omega(J_1)]^2} \right|^2, \quad (\text{F1})$$

with the coupling functions, $\mathcal{U}^{(1)}$ and $\mathcal{U}^{(2)}$, defined in Appendix B of [44]. In Eq. (40), the sum over the resonance vectors (k_1, k_2) is restricted to those such that k_1, k_2 , as well as $k_1 + k_2$ are all non-zero. Importantly, we emphasise that $|\Lambda_{k_1 k_2}(\mathbf{J})|^2$ is independent of N and q .

Small-scale contributions. In Fig. 12, we present the contributions from small scales to the $1/N^2$ relaxation rate. Starting from Eq. (40), let us place ourselves in the limit where the three actions, \mathbf{J} , involved in the three-body resonance condition are close to one another, and assume that $k_1, k_2 \simeq k$. Then, from eq. (B1) in [44], we find that $\mathcal{U}_{k_1 k_2}^{(1)} \simeq k^2 U_k^2$, where we assumed that computing gradients of the form $\partial_J U_{k_1}(J, J')$ does not lead to any additional scaling dependence with respect to k . Assuming local resonances, we may follow Eq. (B3b) and impose the scaling $U_k \simeq k^{-1}$. We then obtain $\mathcal{U}_{k_1 k_2}^{(1)} \simeq 1$ as a function of k . Similarly, starting from eq. (B2) in [44], we find $\mathcal{U}_{k_1 k_2}^{(2)} \simeq k^{-1}$. With these two scalings, we find from Eq. (F1) that $|\Lambda_{k_1 k_2}(\mathbf{J})|^2 \simeq k^{-4}$. Injecting this dependence in Eq. (40), and using the definition from Eq. (44), we get $\mathcal{R}_2(J, k_1, k_2) \simeq k^{-3}$. Finally, we may perform the sum over k_1, k_2 in Eq. (44), with the constraint $\text{Max}[|k_1|, |k_2|] = k$, to obtain $\mathcal{R}_2(J, k) \simeq k^{-2}$. This is the scaling that is indeed recovered in Fig. 12. As expected, in that figure, we also recover that softening accelerates the decay of the contributions stemming from small scales.

Computing the kinetic prediction. In order to evaluate Eq. (40), we need to compute an integral of the form

$$I = \mathcal{P} \int_{J_-}^{J_+} dJ_1 f(J, J_1), \quad (\text{F2})$$

where the integration boundaries $J_{\pm} = J_0 \pm \sigma_0$ follow from Eq. (6). This integral can be rewritten as

$$I(J) = \mathcal{P} \left[\int_0^{J-J_-} d\Delta f(J, J-\Delta) + \int_0^{J_+-J} d\Delta f(J, J+\Delta) \right]. \quad (\text{F3})$$

It subsequently becomes

$$I(J) = \int_0^{\text{Max}[\Delta_-, \Delta_+]} d\Delta \left(f(J, J-\Delta) \Theta[\Delta \leq \Delta_-] + f(J, J+\Delta) \Theta[\Delta \leq \Delta_+] \right), \quad (\text{F4})$$

where we introduced the boundaries $\Delta_- = J - J_-$ and $\Delta_+ = J_+ - J$. With this rewriting, the Cauchy principal value has been safely dealt with. In practice, we finally compute Eq. (F4) using the midpoint rule with the fixed step distance $\Delta_s = (J_+ - J_-)/N_s$ with $N_s = 1000$. In practice, we truncated the sum over harmonics to $|k_1|, |k_2| \leq 100$ in Eq. (40).

Appendix G: Numerical simulations

Equations of motion. Following Eq. (8), the equations of motion of the point vortices are given by

$$\frac{d\mathbf{r}_i}{dt} = \left. \frac{d\mathbf{r}_i}{dt} \right|_{\text{ext}} + \left. \frac{d\mathbf{r}_i}{dt} \right|_{\text{self}}. \quad (\text{G1})$$

Here, $d\mathbf{r}/dt|_{\text{ext}}$ is the contribution from the background external potential, U_{ext} , in Eq. (8). Since it is axisymmetric, following Eq. (5), we can compute $\Omega_i = \Omega(J_i) = dU_{\text{ext}}/dJ_i$, and we find

$$\left. \frac{dx_i}{dt} \right|_{\text{ext}} = \Omega_i y_i, \quad (\text{G2a})$$

$$\left. \frac{dy_i}{dt} \right|_{\text{ext}} = -\Omega_i x_i. \quad (\text{G2b})$$

For the self-interaction part, $d\mathbf{r}_i/dt|_{\text{self}}$, following Eq. (4), we obtain

$$\left. \frac{dx_i}{dt} \right|_{\text{self}} = -\frac{G}{2\pi} \sum_{j \neq i} \gamma_j \frac{y_i - y_j}{(x_i - x_j)^2 + (y_i + y_j)^2 + \epsilon^2}, \quad (\text{G3a})$$

$$\left. \frac{dy_i}{dt} \right|_{\text{self}} = \frac{G}{2\pi} \sum_{j \neq i} \gamma_j \frac{x_i - x_j}{(x_i - x_j)^2 + (y_i - y_j)^2 + \epsilon^2}. \quad (\text{G3b})$$

In practice, we fixed the softening length to $\epsilon/J_0 = 0.01$ in all the simulations considered. The present system has two global invariants, the total energy, $E_{\text{tot}} = H_{\text{tot}}$, as well as the total momentum, $L_{\text{tot}} = \sum_{i=1}^N \gamma_i r_i^2$. We emphasise that evaluating Eq. (G3) is costly, since it requires to perform $\mathcal{O}(N^2)$ computations per evaluation of the rates of change.

Time integration. The Hamiltonian from Eq. (8) is not under a separable form. As such, one cannot readily use standard splitting methods to devise symplectic integration [see, e.g. 65]. This could be circumvented by appropriately “duplicating phase space” [see, e.g., 66]. Though, such symplectic approaches typically require one to carefully tune some “binding constant” between

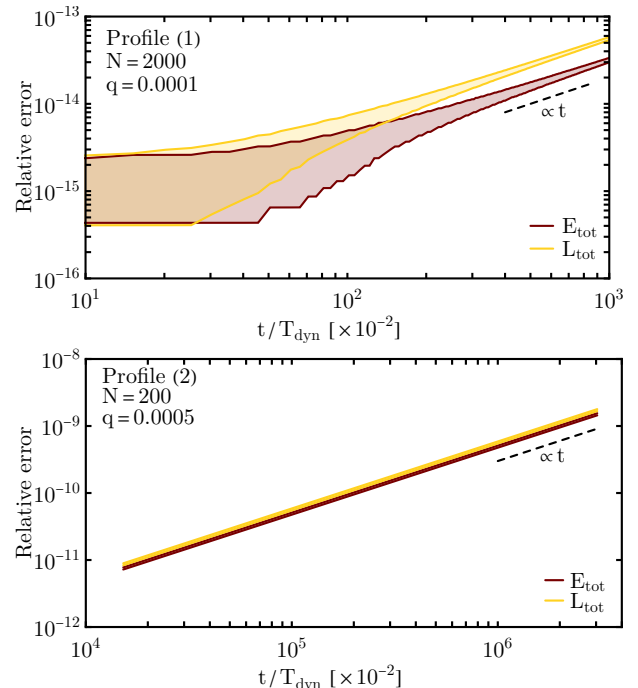


FIG. 16: Time evolution of the relative error in E_{tot} and L_{tot} for profile (1) (top panel) and profile (2) (bottom panel) during the N -body integration. The fillings illustrate the spread between the 16% and 84% level lines over the available realisations.

the two copies of the system’s Hamiltonian. For a given problem, the optimal value of this ad hoc constant, noted ω in [66], can depend, among other things, on the value of N or the considered active fraction, q . In the present context, since we are exploring a large range of values in N , and since both the external potential and the pairwise interaction potentials are smooth, it appears more convenient to resort to more traditional high-order explicit Runge–Kutta methods. In particular, this allows for the use of a large individual timestep making long-time integrations easier to perform. This also removes the need for any additional control parameter to be calibrated. In that view, we used the 15-stage 9th-order “more efficient” **Vern9** method available through the library **OrdinaryDiffEq.jl**.

Simulation setups. Given that we are going to perform numerical simulations over some large ranges in N and q , it is important to carefully pick the parameters of the simulations.

For profile (1), we fixed the timestep to $h/T_{\text{dyn}} \simeq 1.41 \times 10^{-2}$. Each simulation was integrated up to $T_{\text{max}}/T_{\text{dyn}} \simeq 1.013 \times 10^3$ $(0.0001/q)^2 (N/2000)$, to match the scaling of the relaxation time expected from Eq. (19). We made 2000 dumps of each realisation as the integration was performed. The final relative errors on E_{tot} and L_{tot} were typically of order 10^{-13} , as illustrated in Fig. 16. In that same figure, we recover

that our explicit integration scheme leads to a linear growth in time of the error in the global N -body invariants. In practice, the case $(N, q) = (2000, 0.0001)$ presented in Fig. 5 required ~ 40 min of computation time per realisation, on a single core. Of course, simulating the case $(N, q) = (8000, 0.0001)$, explored in Fig. 9, was even more numerically costly, and required ~ 36 h of computation time per realisation.

For profile (2), we fixed the timestep to $h/T_{\text{dyn}} \simeq 1.90 \times 10^{-2}$. Each simulation was integrated up to $T_{\text{max}}/T_{\text{dyn}} \simeq 3.040 \times 10^6 (0.0005/q)^4 (N/200)^2$, to match the scaling from Eq. (41). Similarly, we made 2000 dumps of each realisation as the integration was performed. For that profile, the final relative errors on E_{tot} and L_{tot} were of order 10^{-9} , as illustrated in Fig. 16. In practice, the case $(N, q) = (200, 0.0005)$ presented in Fig. 13 required ~ 21 h of computation time, per realisation, on a single core.

Measuring relaxation. To obtain the numerical results presented throughout the main text, we proceeded as follows. For each realisation, we sliced the action domain, $0.8 \leq J/J_0 \leq 1.2$ in 50 locations, uniformly separated. Then, for each such action, and each dump, we computed the instantaneous number of particles with action smaller than the considered action. Doing so, for each realisation and each considered action, we had at our disposal a time series of $t \mapsto N(< J, t)$, as introduced in Eq. (20a). For each value of (N, q) considered, we ran a total of $N_{\text{real}} = 4096$ independent realisations in order to estimate ensemble averages. In Fig. 17, we illustrate the typical change in the number of particles, $\Delta N(< J, t) = N(< J, t) - N(< J, t=0)$, when averaged over all available realisations. In that figure, we note that the relative change in the fraction of particles is of order 10^{-3} , i.e. we purposely limited our measurements to the onset of relaxation. Nonetheless, such a relative change is much larger than the typical relative error in the N -body invariants (see Fig. 16). This strengthens our confidence in the appropriate convergence of the N -body measurements of the relaxation rate.

Once the average time series $t \mapsto \langle N(< J, t) \rangle$ determined, we performed a linear fit of the form

$$\langle N(< J, t) \rangle \simeq \alpha + \beta t. \quad (\text{G4})$$

Finally, we use the slope β in Eqs. (20a) and (42) to estimate the relaxation rates. Given the computing cost associated with each such realisation, the number of independent realisations, as well as the large number of values of (N, q) considered, obtaining Fig. 9 was no light numerical endeavour. Finally, to obtain Fig. 10, we binned the action domain in bins of width $10^{-2} J_0$.

Bootstraps. In practice, it is essential to estimate the uncertainties associated with these measurements. To that purpose, we use bootstraps. A given bootstrap proceeds as follows. For every value of (N, q) , we perform the ensemble average of $N(< J, t)$ over a sample of N_{real} realisations drawn, with repetitions, from the N_{real} realisations available. Using the associated $\langle N(< J, t) \rangle$, we

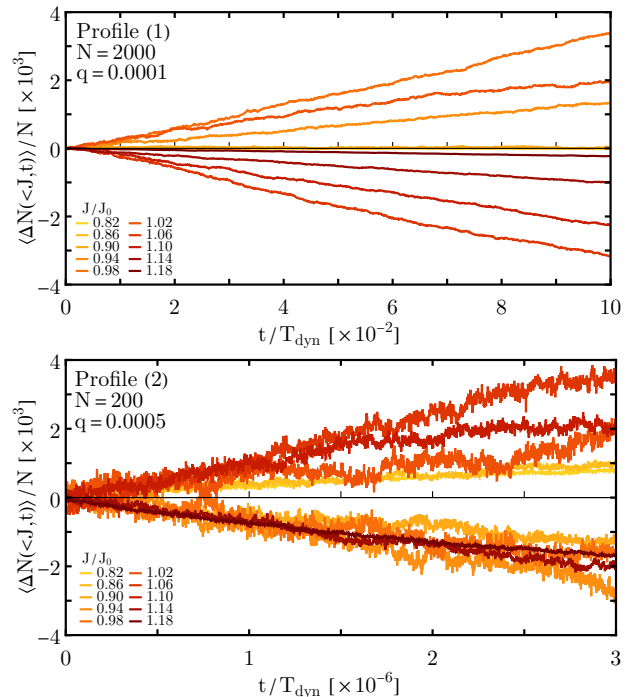


FIG. 17: Time evolution of the number of particles, $N(< J, t)$, in numerical simulations, when averaged over all available realisations, for profile (1) [top] and profile (2) [bottom]. Different colours correspond to different actions J . The linear dependence of these time series is the sign of the onset of relaxation.

perform the linear fit from Eq. (G4) from which we also estimate the variance of the slope β . Finally, for each (N, q) and each considered action, we can draw a value of β according to the associated Gaussian distribution. In practice, we performed a total of 1000 bootstrap measurements, with which we could obtain the 16% and 84% level contours presented in Figs. 5 and 13, as well as the median values presented in Figs. 8 and 14.

Diffusion coefficients. In order to measure the diffusion coefficients in Figs. 5, 7, we proceeded as follows. We start from the exact same setup as in the previous N -body runs, using $N=2000$ and $q=0.0001$. We add to each simulation 1000 zero-mass test particles, which, therefore, do not contribute the system's instantaneous potential. Initially, these particles are all sampled with the same initial action, J_{test} , and with their initial angle, θ , drawn uniformly within $[0, 2\pi]$. In practice, we considered sets of initial conditions with $0.8 \leq J_{\text{test}}/J_0 \leq 1.2$ in increments of $10^{-3} J_0$. For each such choice of J_{test} , we performed 512 independent realisations. Finally, using the same integration parameters as previously (timestep, number of dumps, etc.), for each realisation, we record the time series of $t \mapsto \langle (J(t) - J(0))^2 \rangle$, averaged over all the test particles from that realisation. In Fig. 18, we illustrate such a time series, once averaged over all available realisations. In that figure, we note a transition be-

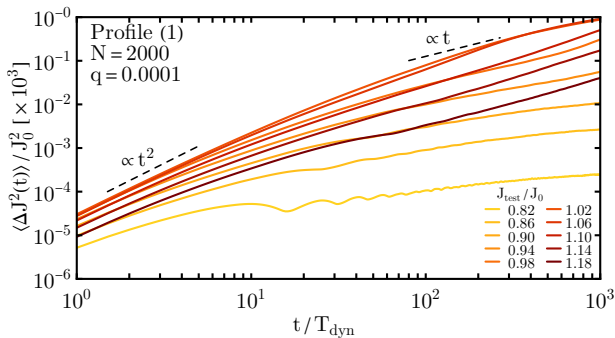


FIG. 18: Time evolution of the (squared) change in action, $\langle \Delta J^2(t) \rangle$, of test particles in numerical simulations, when averaged over all available realisations, for profile (1). Different colours correspond to different initial actions, J_{test} , for the test particles. The diffusion of the test particles shows the transition from a ballistic regime ($\propto t^2$) at early times to a diffusive one ($\propto t$) at late times.

tween an initial “ballistic” regime, during which $\langle \Delta J^2(t) \rangle$ grows like t^2 , and a “diffusive” regime during which it only grows like t . In Fig. 18, we find that the typical relative change in $\langle \Delta J^2 \rangle / J_0^2$ at the end of the integration is, at minimum, of order 10^{-7} . This is much larger than 10^{-13} , the typical relative error in the N -body invariants (see Fig. 16). This brings some confidence in the appropriate convergence of the N -body measurements of the diffusion coefficients.

In order to measure the diffusion coefficient, we estimate the numerical diffusion coefficient, D_{num} , through the slope

$$D_{\text{num}}(J_{\text{test}}) = \frac{\langle \Delta J^2(t_{\text{max}}) \rangle - \langle \Delta J^2(t_{\text{min}}) \rangle}{t_{\text{max}} - t_{\text{min}}}, \quad (\text{G5})$$

between the times t_{min} and t_{max} . For Fig. 5, in order not to be polluted by the initial ballistic regime (Fig. 18), we considered the time range $t_{\text{min}} = 500 T_{\text{dyn}}$ and $t_{\text{max}} = 1000 T_{\text{dyn}}$. We checked that varying slightly these values did not lead to any significant change in the measured D_{num} . For the finite-time diffusion coefficients presented in Fig. 7, we fixed $t_{\text{min}} = 0$ and used the values of t_{max} indicated in that figure. In both figures, uncertainties are estimated using bootstrap resamplings. This amounts to performing 1 000 different ensembles averages over sets of 512 realisations, but allowing for repetitions. In Figs. 5 and 7, we present the 16% and 84% level contours over these bootstraps.

Appendix H: Properties of the regularised Landau equation

In this Appendix, we study the properties of the regularised Landau equation from Eq. (32). In particular, we show how resonance broadening regularises the divergences of the Landau diffusion coefficient for 2D point

vortices.

1. Regularisation of the logarithmic divergence of the Landau diffusion coefficient

Let us first consider the case of a monotonic frequency profile, or a value of J far from the value J_* , where the frequency profile has an extremum.

The regularised diffusion coefficient is given by Eq. (33). Using the expression of the unsoftened potential of interaction from Eq. (B3) and the identity $\sum_{k>0} x^k/k = -\ln(1-x)$, we can explicitly perform the sum over k in the function $\Lambda_{\text{tot}}(J, J_1)$ [34], and obtain

$$D(J) = -\frac{1}{2}\gamma \int_0^{+\infty} dJ_1 \ln \left(1 - \frac{J_{\text{min}}}{J_{\text{max}}} \right) \times \delta_{T_{\text{reg}}} [\Omega(J) - \Omega(J_1)] F(J_1), \quad (\text{H1})$$

with $J_{\text{min}} = \text{Min}[J, J_1]$ and similarly for J_{max} .

When $T_{\text{reg}} \rightarrow +\infty$, the Lorentzian tends to a Dirac delta imposing $\Omega(J_1) = \Omega(J)$, hence $J_1 = J$. In that case, the (Landau) diffusion coefficient diverges logarithmically at small scales, i.e. for $k \rightarrow +\infty$. Introducing a cut-off k_{max} , and using Eq. (23), we obtain [34]

$$D(J) = \frac{1}{2}\gamma \frac{F(J)}{|\Omega'(J)|} \ln \Lambda, \quad (\text{H2})$$

with $\ln \Lambda = \sum_{k>0} \frac{1}{k} \sim \ln k_{\text{max}}$. When T_{reg} is finite, there is no divergence in Eq. (H1).

Let us now assume that T_{reg} is sufficiently large. In that case, the regularised Dirac delta (Lorentzian) is strongly peaked around $J_1 = J$. We can therefore make a local approximation and expand $\Omega(J_1)$ to first order around J . We can also replace $F(J_1)$ by $F(J)$. Doing so, at leading order, we obtain

$$D(J) \sim -\frac{1}{2}\gamma F(J) J \int_{-\infty}^{+\infty} dx \ln |x| \delta_{T_{\text{reg}}} [\Omega'(J) J x], \quad (\text{H3})$$

giving

$$D(J) \sim \frac{1}{2}\gamma \frac{F(J)}{|\Omega'(J)|} \ln [T_{\text{reg}} |\Omega'(J) J|. \quad (\text{H4})$$

We thus find that the regularized Coulomb logarithm, $\ln \Lambda$, is equal to the logarithm of the ratio between T_{reg} and the timescale $1/(|\Omega'(J) J|)$ set by the shear of the frequency profile.

2. Regularisation of the Landau diffusion coefficient when $J = J_*$

We now consider the case where the frequency profile has a minimum at J_* , i.e. one has $\Omega'_* = \Omega'(J_*) = 0$. In that case, the Landau diffusion coefficient diverges at $J = J_*$,

as discussed in the main text (see also Eq. H2). Resonance broadening, which is here accounted for heuristically by a finite value of T_{reg} , regularises this divergence. Let us consider the function $D_{\star}(T_{\text{reg}})$ obtained by taking $J=J_{\star}$ in Eq. (H1).

For $T_{\text{reg}} \gg T_{\text{reg}}^c$ (with the transition timescale T_{reg}^c to be introduced in Eq. H10), and using the same method as above but pushing the Taylor expansion up to second order (assuming $\Omega_{\star}'' = \Omega''(J_{\star}) \neq 0$), we find at leading order

$$D_{\star} \sim -\frac{1}{2}\gamma F_{\star} J_{\star} \int_{-\infty}^{+\infty} dx \ln|x| \delta_{T_{\text{reg}}} \left[\frac{1}{2} \Omega_{\star}'' J_{\star}^2 x^2 \right], \quad (\text{H5})$$

giving

$$D_{\star} \sim \frac{1}{8}\gamma F_{\star} \sqrt{\frac{T_{\text{reg}}}{|\Omega_{\star}''|}} \left\{ \pi + 2 \ln \left[\frac{1}{2} |\Omega_{\star}''| J_{\star}^2 T_{\text{reg}} \right] \right\}. \quad (\text{H6})$$

Ignoring logarithmic corrections, and using $\Gamma \sim F_{\star} J_{\star}$, we obtain the scaling

$$D_{\star} \sim \gamma \Gamma \sqrt{\frac{T_{\text{reg}}}{J_{\star}^2 |\Omega_{\star}''|}} \propto T_{\text{reg}}^{1/2}. \quad (\text{H7})$$

This scaling remains valid for a softened potential.

For $T_{\text{reg}} \ll T_{\text{reg}}^c$, using $\delta_{T_{\text{reg}}}(\omega) \rightarrow T_{\text{reg}}/\pi$, we obtain

$$D_{\star} \sim -\frac{1}{2}\gamma \frac{T_{\text{reg}}}{\pi} \int_0^{+\infty} dJ_1 \ln \left(1 - \frac{J_{\min}}{J_{\max}} \right) F(J_1), \quad (\text{H8})$$

yielding the scaling

$$D_{\star} \sim \gamma \Gamma T_{\text{reg}} \propto T_{\text{reg}}. \quad (\text{H9})$$

Once again, this scaling remains valid for a softened potential. The transition between these two regimes occurs at

$$T_{\text{reg}}^c \sim \frac{1}{J_{\star}^2 |\Omega_{\star}''|}, \quad D_{\star}^c \sim \frac{\gamma \Gamma}{J_{\star}^2 |\Omega_{\star}''|}. \quad (\text{H10})$$

We note that the value of T_{reg}^c is independent of N . Since T_{reg} increases with N , we expect that we are generically in the regime $T_{\text{reg}} \gg T_{\text{reg}}^c$, not in the regime $T_{\text{reg}} \ll T_{\text{reg}}^c$.

3. Self-consistent relation

In the main text, T_{reg} was treated as an adjustable parameter, see e.g., Fig. 6. Now, if we assume the relation

$$T_{\text{reg}} \sim \frac{J_{\star}^2}{D_{\star}}, \quad (\text{H11})$$

and use Eq. (H1) with $J=J_{\star}$, we can obtain the expression of T_{reg} (or D_{\star}) self-consistently. We refer to Appendix I for a graphical study.

For $T_{\text{reg}} \gg T_{\text{reg}}^c$ (i.e. for $D_{\star} \gg D_{\star}^c$), combining Eqs. (H7) and (H11), we get

$$D_{\star} \sim \left(\frac{\gamma \Gamma}{\sqrt{|\Omega_{\star}''|}} \right)^{2/3}, \quad T_{\text{reg}} \sim J_{\star}^2 \left(\frac{\sqrt{|\Omega_{\star}''|}}{\gamma \Gamma} \right)^{2/3}. \quad (\text{H12})$$

This gives $T_{\text{reg}} \propto D_{\star}^{-1} \propto \gamma^{-2/3} \propto N^{2/3}$. To the best of our knowledge, such a $N^{2/3}$ scaling has not been reported before.

For $T_{\text{reg}} \ll T_{\text{reg}}^c$ (i.e. for $D_{\star} \ll D_{\star}^c$), combining Eqs. (H9) and (H11), we get

$$D_{\star} \sim J_{\star} \sqrt{\gamma \Gamma}, \quad T_{\text{reg}} \sim \frac{J_{\star}}{\sqrt{\gamma \Gamma}}, \quad (\text{H13})$$

giving $T_{\text{reg}} \sim D_{\star}^{-1} \sim \gamma^{-1/2} \sim N^{1/2}$. This is the $N^{1/2}$ scaling presented in the main text, which implicitly assumed $T_{\text{reg}} \ll T_{\text{reg}}^c$ (see Section III E). It corresponds to the Taylor-McNamara [55] scaling which applies to an unsheared flow (see Appendix I3). In the case considered in [55], $\Omega(J)$ is constant, so that $\Omega''(J)$ vanishes everywhere, as well as all its higher order derivatives. This implies $T_{\text{reg}}^c \rightarrow +\infty$ and $D_{\star}^c \rightarrow 0$, following Eq. (H10). By contrast, when $\Omega_{\star}'' \neq 0$, as in our case, there exists another regime, $T_{\text{reg}} \gg T_{\text{reg}}^c$, that yields a $N^{2/3}$ scaling. It could be that this scaling, which is valid when $|\Omega_{\star}''| \gg \sqrt{\gamma \Gamma}/J_{\star}^3 \sim 1/\sqrt{N}$, is more relevant than the $N^{1/2}$ scaling, valid in the opposite limit, presented in the main text. Unfortunately, these two scalings cannot be distinguished in the numerical simulations presented here, since $2/3$ is close to $1/2$. This subtle distinction will be considered in a future work, by studying a simpler system for which more precise numerical simulations can be performed.

Remark. One can generalise the previous results to the case where the first $n-1$ derivatives of $\Omega(J)$ vanish at J_{\star} but $\Omega_{\star}^{(n)} = \Omega^{(n)}(J_{\star}) \neq 0$. Instead of Eq. (H7), we find

$$D_{\star} \sim \frac{\gamma \Gamma T_{\text{reg}}^{1-1/n}}{J_{\star} |\Omega_{\star}^{(n)}|^{1/n}} \quad (\text{H14})$$

for $T_{\text{reg}} \gg 1/(J_{\star}^n |\Omega_{\star}^{(n)}|)$. Then, instead of Eq. (H12), we find

$$T_{\text{reg}} \sim \frac{J_{\star}^2}{D_{\star}} \sim \left[\frac{J_{\star}^3 |\Omega_{\star}^{(n)}|^{1/n}}{\gamma \Gamma} \right]^{\frac{1}{2-1/n}} \quad (\text{H15})$$

for $|\Omega_{\star}^{(n)}| \gg \sqrt{\gamma \Gamma}/J_{\star}^{n+1} \sim 1/\sqrt{N}$. This yields the general scaling $T_{\text{reg}} \sim D_{\star}^{-1} \sim \gamma^{-1/(2-1/n)} \sim N^{1/(2-1/n)}$. The results from Eqs. (H8) and (H13), corresponding to the Taylor-McNamara regime [55], are not changed. For $n=1$ we recover the Landau scaling, for $n=2$ we recover the new scaling from Eq. (H12), and for $n \rightarrow +\infty$ we recover the Taylor-McNamara [55] scaling. Exploring these different regimes of relaxation will be the topic of a future work.

Appendix I: Resonance broadening from stochastic equations of motion

In this Appendix, we introduce an alternative stochastic model to justify the heuristic resonance broadening from Section III E and motivate the regularisation of the Dirac delta by a Lorentzian function (Eq. 31). In addition, we use this model to estimate the diffusion coefficient of point vortices. We also point out the limitations of this approach and the need for a more refined kinetic framework. Finally, we discuss the connection between this work and previous literature.

1. Regularised Landau equation from individual stochastic equations

When derived from the BBGKY hierarchy at order $1/N$, the Landau equation generically reads [43]

$$\begin{aligned} \frac{\partial F(J, t)}{\partial t} = & \frac{\partial}{\partial J} \left[\int_0^{+\infty} d\tau \int_0^{+\infty} dJ_1 \int_0^{2\pi} d\theta_1 \right. \\ & \times \langle \mathcal{F}(1 \rightarrow 0, t) G(t, t-\tau) \mathcal{F}(1 \rightarrow 0, t-\tau) \rangle \\ & \left. \times \left(\frac{\partial}{\partial J} - \frac{\partial}{\partial J_1} \right) F(J, t) \frac{1}{\gamma} F(J_1, t) \right], \quad (\text{I1}) \end{aligned}$$

where

$$\mathcal{F}(1 \rightarrow 0, s) = -i\gamma \sum_k k e^{ik[\theta(s) - \theta_1(s)]} U_k(J, J_1) \quad (\text{I2})$$

is the force (velocity) created by particle (vortex) 1 on particle (vortex) 0 at time s , and $G(t, t-\tau)$ is an appropriate Green function taking into account the motion of the particles between t and $t-\tau$ [43]. In Eq. (I1), the brackets indicate an average over the fluctuating trajectories of the particles (see below). To calculate the temporal correlation function in Eq. (I1), one usually assumes that the particles follow the unperturbed mean field trajectories at leading order. This leads to the Landau equation (Eq. 14). However, this approximation breaks down notably close to an extremum of $\Omega(J)$, i.e. when particles have similar frequencies. In that case, one has to take into account fluctuations in the particles' individual trajectories.

Following [30], we replace the deterministic equations of motion by effective stochastic equations where the amplitude of the noise term is determined by the diffusion coefficient obtained from the kinetic theory itself (see below). Assuming that the diffusion is isotropic [30], we then have $D_{\theta\theta}(J) = D(J)/(4J^2)$, where $D(J) \equiv D_{JJ}(J)$ [resp. $D_{\theta\theta}(J)$] is the diffusion coefficient in action [resp. angle].

Since our goal is to illustrate the origin of resonance broadening in a simple manner, we make the following approximations: (i) We assume that the stochastic process can be described by a Gaussian white noise; (ii) We ignore the diffusion in action in the stochastic equations

of motion; (iii) We assume that the diffusion coefficient in angle, $D_{\theta\theta}$, is constant with value $D_*/(4J_*^2)$, where $D_* = D(J_*)$ is the action diffusion coefficient at the extremum of the frequency profile. As a result, we approximate the motion of the particles with the effective stochastic equations

$$\frac{dJ}{dt} = 0, \quad (\text{I3a})$$

$$\frac{d\theta}{dt} = \Omega(J) + \sqrt{D_*/(4J_*^2)} \eta(t), \quad (\text{I3b})$$

where $\eta(t)$ is a Gaussian white noise such that $\langle \eta(t) \rangle = 0$ and $\langle \eta(t) \eta(t') \rangle = \delta_D(t-t')$. Integrating these equations between t and $t-\tau$, we obtain the stochastic trajectories

$$J(t-\tau) = J, \quad (\text{I4a})$$

$$\theta(t-\tau) = \theta - \Omega(J)\tau - \sqrt{D_*/(4J_*^2)} \int_0^\tau dt' \eta(t-t'). \quad (\text{I4b})$$

Substituting these solutions into Eq. (I1) and carrying out the integration over θ_1 , we obtain

$$\begin{aligned} \frac{\partial F(J, t)}{\partial t} = & 4\pi\gamma \frac{\partial}{\partial J} \left[\int_0^{+\infty} dJ_1 \int_0^{+\infty} d\tau \sum_{k>0} k^2 |U_k(J, J_1)|^2 \right. \\ & \times e^{ik\Delta\Omega(J, J_1)\tau} \left\langle e^{ik\sqrt{D_*/(4J_*^2)} \int_0^\tau dt' [\eta(t-t') - \eta_1(t-t')]} \right\rangle \\ & \left. \times \left(\frac{\partial}{\partial J} - \frac{\partial}{\partial J_1} \right) F(J, t) F(J_1, t) \right], \quad (\text{I5}) \end{aligned}$$

where we introduced the frequency difference, $\Delta\Omega(J, J_1) = \Omega(J) - \Omega(J_1)$. Now, if we assume a Gaussian distribution for the fluctuations, we have [30]

$$\left\langle e^{ik\sqrt{D_*/(4J_*^2)} \int_0^\tau dt' \eta(t-t')} \right\rangle = e^{-k^2 D_*/(8J_*^2)\tau}, \quad (\text{I6})$$

and the kinetic equation (Eq. I1) becomes

$$\begin{aligned} \frac{\partial F(J, t)}{\partial t} = & 4\pi\gamma \frac{\partial}{\partial J} \left[\int_0^{+\infty} dJ_1 \int_0^{+\infty} d\tau \sum_{k>0} k^2 |U_k(J, J_1)|^2 \right. \\ & \left. \times e^{ik\Delta\Omega(J, J_1)\tau} e^{-\tau/T_k} \left(\frac{\partial}{\partial J} - \frac{\partial}{\partial J_1} \right) F(J, t) F(J_1, t) \right], \quad (\text{I7}) \end{aligned}$$

where we introduced the (scale-dependent) decorrelation time

$$T_k = \frac{4J_*^2}{D_* k^2}. \quad (\text{I8})$$

Integrating Eq. (I7) over τ , we obtain

$$\begin{aligned} \frac{\partial F(J, t)}{\partial t} = & 4\pi^2\gamma \frac{\partial}{\partial J} \left[\int_0^{+\infty} dJ_1 \sum_{k>0} k^2 |U_k(J, J_1)|^2 \right. \\ & \left. \times \delta_{T_k}(k \Delta\Omega[J, J_1]) \left(\frac{\partial}{\partial J} - \frac{\partial}{\partial J_1} \right) F(J, t) F(J_1, t) \right], \quad (\text{I9}) \end{aligned}$$

with $\delta_{T_k}(\omega)$ the broadened Dirac delta from Eq. (31).¹⁰ Explicitly, the kinetic equation reads

$$\frac{\partial F(J, t)}{\partial t} = 4\pi\gamma \frac{\partial}{\partial J} \left[\int_0^{+\infty} dJ_1 \sum_{k>0} k^2 |U_k(J, J_1)|^2 \right. \\ \left. \times \frac{T_k}{1+(k \Delta\Omega[J, J_1] T_k)^2} \left(\frac{\partial}{\partial J} - \frac{\partial}{\partial J_1} \right) F(J, t) F(J_1, t) \right]. \quad (\text{I10})$$

If we let $T_k \rightarrow +\infty$, or if $k \Delta\Omega T_k \gg 1$, which both amount to neglecting the fluctuations in particles individual trajectories, Eq. (I10) becomes the Landau equation (Eq. 14). This is valid if we are far from the extremum of $\Omega(J)$.

However, when J is close to J_* , we are faced with the opposite limit, namely $k \Delta\Omega T_k \ll 1$. In that case, the kinetic equation (Eq. I10) reduces to

$$\frac{\partial F(J, t)}{\partial t} = 4\pi\gamma \frac{\partial}{\partial J} \left[\int_0^{+\infty} dJ_1 \sum_{k>0} k^2 |U_k(J, J_1)|^2 \right. \\ \left. \times T_k \left(\frac{\partial}{\partial J} - \frac{\partial}{\partial J_1} \right) F(J, t) F(J_1, t) \right]. \quad (\text{I11})$$

2. Diffusion coefficient at the frequency extremum

The (broadened) Landau equation (Eq. I9) can be viewed as a Fokker–Planck equation in action space involving a diffusion term and a drift term. The diffusion coefficient in action reads

$$D(J) = 8\pi^2\gamma \int_0^{+\infty} dJ_1 \sum_{k>0} k^2 |U_k(J, J_1)|^2 \\ \times \delta_{T_k}(k \Delta\Omega[J, J_1]) F(J_1, t). \quad (\text{I12})$$

As expected, when $T_k \rightarrow +\infty$, this equation reduces to the usual Landau diffusion coefficient (Eq. 17), which scales like $1/N$ via the prefactor γ . This limit is relevant if we are sufficiently far from the extremum of frequency. In that case [31, 37], we get

$$D(J) = 8\pi^2\gamma \sum_r \sum_{k>0} k |U_k(J, J_r)|^2 \frac{F(J_r, t)}{|\Omega'(J_r)|}, \quad (\text{I13})$$

where J_r are the actions of the resonant particles such that $\Omega(J_r) = \Omega(J)$ (see Eq. 23).

When $J \rightarrow J_*$, following the same argument as in Eq. (24b), the resonance condition has two roots. Assuming that the frequency profile is quadratic about J_* ,

¹⁰ In the main text, we implicitly assumed $T_k = T_{\text{reg}}/k$. This leads to the identity $\delta_{T_k}(k\omega) = \delta_{T_{\text{reg}}}(\omega)/|k|$, similar to the one satisfied by the usual Dirac delta. From this identity results the broadened Landau equation (Eq. 32). Here, the function $\delta_{T_k}(k\omega)$ has a different dependence with k , so the broadened Landau equation (Eq. I9) is slightly different. See [31] for another regularisation of the Dirac delta obtained by integrating over a finite period of time.

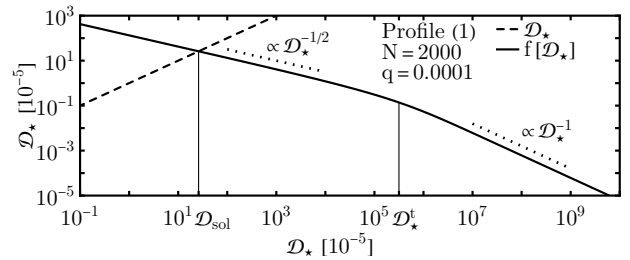


FIG. 19: Illustration of the self-consistent relation, $D_* = f(D_*)$ from Eq. (I16), for profile (1), here using the rescaled diffusion coefficient, D_* , following Eq. (20b). Here, D_*^i illustrates the transition between the two regimes investigated in Appendix H 2. For the case $N=2000$ and $q=0.0001$, the fixed-point solution is found for $D_{\text{sol}} \simeq 2.6 \times 10^6$. This is $\sim 20x$ too large compared to the N -body value estimated in Fig. 5.

these two roots are $J_r = J$ and $J_r = 2J_* - J$, which are symmetric with respect to J_* . As such, when $J \rightarrow J_*$, we obtain

$$D(J) \simeq 16\pi^2\gamma \sum_{k>0} k |U_k(J_*, J_*)|^2 \frac{F(J_*, t)}{|\Omega'(J)|}. \quad (\text{I14})$$

We see that the diffusion coefficient diverges at the extremum of frequency, because of the factor $1/|\Omega'(J)|$. This is the same result as the one obtained in Eq. (25b). When accounting for resonance broadening, this divergence is regularised by the finite value of T_k , just like it was regularised by T_{reg} in Eq. (33), as visible in Fig. 6.¹¹ Unfortunately, the regularisation from Eq. (32) in the main text still involves the adjustable parameter, T_{reg} , that remains to be determined. In Appendix H, we have estimated T_{reg} by heuristically relating T_{reg} to D_* through Eq. (H11). However, this equation was not given a precise justification.

In the present approach, T_k is related to D_* through the similar Eq. (I8), which now arises from a simple stochastic model. Like in Appendix H, one could then hope to obtain the value of T_k self-consistently through D_* (see Eq. I8), by applying Eq. (I12) at $J = J_*$. Indeed, this leads to a self-consistent relation of the form

$$D_* = f[D_*], \quad (\text{I15})$$

with the function

$$f[D_*] = 8\pi^2\gamma \int_0^{+\infty} dJ_1 \sum_{k>0} k^2 |U_k(J_*, J_1)|^2 \\ \times \delta_{T_k}(k \Delta\Omega[J_*, J_1]) F(J_1, t), \quad (\text{I16})$$

¹¹ Similarly, in the absence of softening, $\sum_k k |U_k(J_*, J_*)|^2$ as present in Eq. (I14), diverges logarithmically on small scales (see Fig. 4). Fortunately, given that T_k also depends on k (see Eq. I8), one can show that resonance broadening also regularises this small scale divergence, see Appendix H 1.

where $T_k = T_k[D_\star]$ follows from Eq. (I8). In the present heuristic approach, the self-consistent solution of Eq. (I15) should determine D_\star , hence quantifying the level of resonance broadening occurring in the system.

In Fig. 19, we illustrate the function $D_\star \mapsto f[D_\star]$, with the associated fixed-point search.¹² In that figure, considering the same case as in Fig. 5, we find the fixed-point solution, $D_{\text{sol}} \simeq 2.6 \times 10^6$. This is ~ 20 x larger than the value for D_\star effectively measured in the numerical simulations. This shows the limitation of the simple stochastic model presented in this Appendix. Surely a refined description of the present resonant broadening is required, e.g., by considering more intricate individual stochastic equations of motion (Eq. I3).

3. Link with previous works

The simplified model from Eq. (I9) allows us to draw some connections between the Landau diffusion coefficient of sheared flows [23, 24, 30] and the Taylor–McNamara diffusion coefficient of unsheared flows [55]. These correspond to two important limits considered in the literature, each with different scalings with respect to N .

For the sake of simplicity, let us assume that the vorticity and frequency profiles are approximately flat on a domain of size J_\star , writing $F \simeq F_\star$ and assuming $k \Delta\Omega T_k \ll 1$. From Eq. (I12), we obtain

$$D^2 \simeq 32\pi\gamma J_\star^2 F_\star \int_0^{J_\star} dJ_1 \sum_{k>0} |U_k(J, J_1)|^2. \quad (\text{I17})$$

Since $\gamma \sim 1/N$, we recover the Taylor–McNamara scaling [55], $D \sim 1/\sqrt{N}$. If we account for an active fraction of particles, as in the main text, this scaling becomes $D \sim q/\sqrt{N}$.

The integral in Eq. (I17) can be estimated analytically when using the (unsoftened) interaction potential from Eq. (B3). It leads to

$$D^2 \simeq \frac{2J_\star^3}{\pi} \gamma F_\star, \quad (\text{I18})$$

up to logarithmic corrections. To make the connection with the results of Taylor–McNamara [55], we introduce the original isotropic diffusion coefficient in the physical space, (x, y) , via $D_{\text{iso}} \sim D/(2J_\star)$, as well as the total circulation $\Gamma \sim 2\pi F_\star J_\star$. We obtain

$$D_{\text{iso}}^2 \simeq \frac{J_\star}{2\pi} \gamma F_\star \sim \frac{1}{4\pi^2} \Gamma \gamma \sim \frac{1}{4\pi^2} N \gamma^2. \quad (\text{I19})$$

¹² This function has the same asymptotic behaviours, $f(D_\star) \propto D_\star^{-1/2}$ for $D_\star \ll D_\star^t$ and $f(D_\star) \propto D_\star^{-1}$ for $D_\star \gg D_\star^t$ with $D_\star^t \sim J_\star^2/T_{\text{reg}}^c \sim J_\star^4/|\Omega_\star''|$, as the equivalent function studied in Appendix H with a simpler model. Therefore, the discussion of Appendix H on the different regimes also applies to the present situation.

Of course, following our numerous approximations, the prefactor of Eq. (I19) is uncertain by a factor of order unity. Nonetheless, this should be compared with the Taylor–McNamara formula, $D_{\text{TN}}^2 = N\gamma^2/(16\pi^3)$ [55]. Our estimate of D_{iso} turns out to be larger than D_{TN} by a factor $\sqrt{4\pi} \sim 3.5$.

-
- [1] P.-H. Chavanis, in *Dynamics and Thermodynamics of Systems with Long-Range Interactions* (Springer, 2002), vol. 602, pp. 208–289.
- [2] F. Bouchet and A. Venaille, *Phys. Rep.* **515**, 227 (2012).
- [3] L. Onsager, *Nuovo Cimento* **6**, 279 (1949).
- [4] E. M. Purcell and R. V. Pound, *Phys. Rev.* **81**, 279 (1951).
- [5] G. Joyce and D. Montgomery, *J. Plasma Phys.* **10**, 107 (1973).
- [6] D. Montgomery and G. Joyce, *Phys. Fluids* **17**, 1139 (1974).
- [7] S. Kida, *J. Stat. Phys. Japan* **39**, 1395 (1975).
- [8] Y. B. Pointin and T. S. Lundgren, *Phys. Fluids* **19**, 1459 (1976).
- [9] T. S. Lundgren and Y. B. Pointin, *J. Stat. Phys.* **17**, 323 (1977).
- [10] G. L. Eyink and K. R. Sreenivasan, *Rev. Mod. Phys.* **78**, 87 (2006).
- [11] J. Miller, *Phys. Rev. Lett.* **65**, 2137 (1990).
- [12] R. Robert and J. Sommeria, *J. Fluid Mech.* **229**, 291 (1991).
- [13] P.-H. Chavanis, J. Sommeria, and R. Robert, *ApJ* **471**, 385 (1996).
- [14] J. Binney and S. Tremaine, *Galactic Dynamics: Second Edition* (Princeton Univ. Press, 2008).
- [15] D. Lynden-Bell, *MNRAS* **136**, 101 (1967).
- [16] P.-H. Chavanis, *Physica A* **365**, 102 (2006).
- [17] D. Lynden-Bell and R. Wood, *MNRAS* **138**, 495 (1968).
- [18] S. Chandrasekhar, *Principles of Stellar Dynamics* (Univ. Chicago Press, 1942).
- [19] S. Chandrasekhar, *ApJ* **97**, 255 (1943).
- [20] S. Chandrasekhar, *ApJ* **97**, 263 (1943).
- [21] S. Chandrasekhar, *Rev. Mod. Phys.* **21**, 383 (1949).
- [22] S. Chandrasekhar, *Rev. Mod. Phys.* **15**, 1 (1943).
- [23] P.-H. Chavanis, *Phys. Rev. E* **58**, R1199 (1998).
- [24] P.-H. Chavanis, *Phys. Rev. E* **64**, 026309 (2001).
- [25] L. D. Landau, *Phys. Z. Sowj. Union* **10**, 154 (1936).
- [26] R. Balescu, *Phys. Fluids* **3**, 52 (1960).
- [27] A. Lenard, *Ann. Phys. (N.-Y.)* **10**, 390 (1960).
- [28] M. N. Rosenbluth, W. M. MacDonald, and D. L. Judd, *Phys. Rev.* **107**, 1 (1957).
- [29] D. H. E. Dubin and T. M. O’Neil, *Phys. Rev. Lett.* **60**, 1286 (1988).
- [30] D. H. E. Dubin, *Phys. Plasmas* **10**, 1338 (2003).
- [31] P.-H. Chavanis and M. Lemou, *Eur. Phys. J. B* **59**, 217 (2007).
- [32] P.-H. Chavanis, *Physica A* **387**, 1123 (2008).
- [33] P.-H. Chavanis, *J. Stat. Mech* **2010**, 05019 (2010).
- [34] P.-H. Chavanis, *J. Stat. Mech.* **2012**, 02019 (2012).
- [35] P.-H. Chavanis, *Physica A* **391**, 3657 (2012).
- [36] J.-B. Fouvry, P.-H. Chavanis, and C. Pichon, *Phys. Lett. A* **380**, 2589 (2016).
- [37] P.-H. Chavanis, *Eur. Phys. J. Plus* **138**, 136 (2023).
- [38] O. C. Eldridge and M. Feix, *Phys. Fluids* **6**, 398 (1962).
- [39] J.-B. Fouvry, B. Bar-Or, and P.-H. Chavanis, *Phys. Rev. E* **100**, 052142 (2019).
- [40] J.-B. Fouvry, P.-H. Chavanis, and C. Pichon, *Phys. Rev. E* **102**, 052110 (2020).
- [41] J. Heyvaerts, *MNRAS* **407**, 355 (2010).
- [42] P.-H. Chavanis, *Physica A* **391**, 3680 (2012).
- [43] P.-H. Chavanis, *A&A* **556**, A93 (2013).
- [44] J.-B. Fouvry, *Phys. Rev. E* **106**, 054123 (2022).
- [45] J.-B. Fouvry and M. Roule, *Phys. Rev. E* **108**, 054108 (2023).
- [46] P. K. Newton, *The N-Vortex Problem: Analytical Techniques* (Springer, 2001).
- [47] P.-H. Chavanis, *Eur. Phys. J. B* **85**, 229 (2012).
- [48] M. Roule, J.-B. Fouvry, C. Pichon, and P.-H. Chavanis, *Phys. Rev. E* **106**, 044118 (2022).
- [49] F. P. C. Benetti and B. Marcos, *Phys. Rev. E* **95**, 022111 (2017).
- [50] M. Antoni and S. Ruffo, *Phys. Rev. E* **52**, 2361 (1995).
- [51] T. M. Rocha Filho, A. E. Santana, M. A. Amato, and A. Figueiredo, *Phys. Rev. E* **90**, 032133 (2014).
- [52] J.-B. Fouvry and B. Bar-Or, *MNRAS* **481**, 4566 (2018).
- [53] J. Weinstock, *Phys. Fluids* **12**, 1045 (1969).
- [54] J. A. Krommes, *Phys. Rep.* **360**, 1 (2002).
- [55] J. B. Taylor and B. McNamara, *Phys. Fluids* **14**, 1492 (1971).
- [56] J. Magorrian, *MNRAS* **507**, 4840 (2021).
- [57] J. Barré and S. Gupta, *J. Stat. Mech.* **2014**, 02017 (2014).
- [58] O. Feliachi and F. Bouchet, *J. Stat. Phys.* **186**, 22 (2022).
- [59] O. Feliachi and J.-B. Fouvry, *Phys. Rev. E* **110**, 024108 (2024).
- [60] A. Rogister and C. Oberman, *J. Plasma Phys.* **2**, 33 (1968).
- [61] C. Hamilton and T. Heinemann, *arXiv* 2011.14812 (2020).
- [62] M. D. Weinberg, *ApJ* **300**, 93 (1986).
- [63] J.-B. Fouvry and S. Prunet, *MNRAS* **509**, 2443 (2022).
- [64] A. J. Kalnajs, *ApJ* **205**, 745 (1976).
- [65] E. Hairer, C. Lubich, and G. Wanner, *Geometric numerical integration: Second Edition* (Springer, 2006).
- [66] M. Tao, *Phys. Rev. E* **94**, 043303 (2016).